

144
10-28-87

(PB)

(2)

I-32301

DR 0329-8

(5)

ORNL/TM-10487

ornl

**OAK RIDGE
NATIONAL
LABORATORY**

MARTIN MARIETTA

**Effect of Rapid Solidification
on Stainless Steel Weld Metal
Microstructures and Its Implications
on the Schaeffler Diagram**

S. A. David
J. M. Vitek
R. W. Reed
T. L. Hebble

OPERATED BY
MARTIN MARIETTA ENERGY SYSTEMS, INC.
FOR THE UNITED STATES
DEPARTMENT OF ENERGY

DISTRIBUTION OF THIS PUBLICATION IS UNLIMITED

Printed in the United States of America. Available from
National Technical Information Service
U.S. Department of Commerce
5285 Port Royal Road, Springfield, Virginia 22161
NTIS price codes—Printed Copy: A04 Microfiche A01

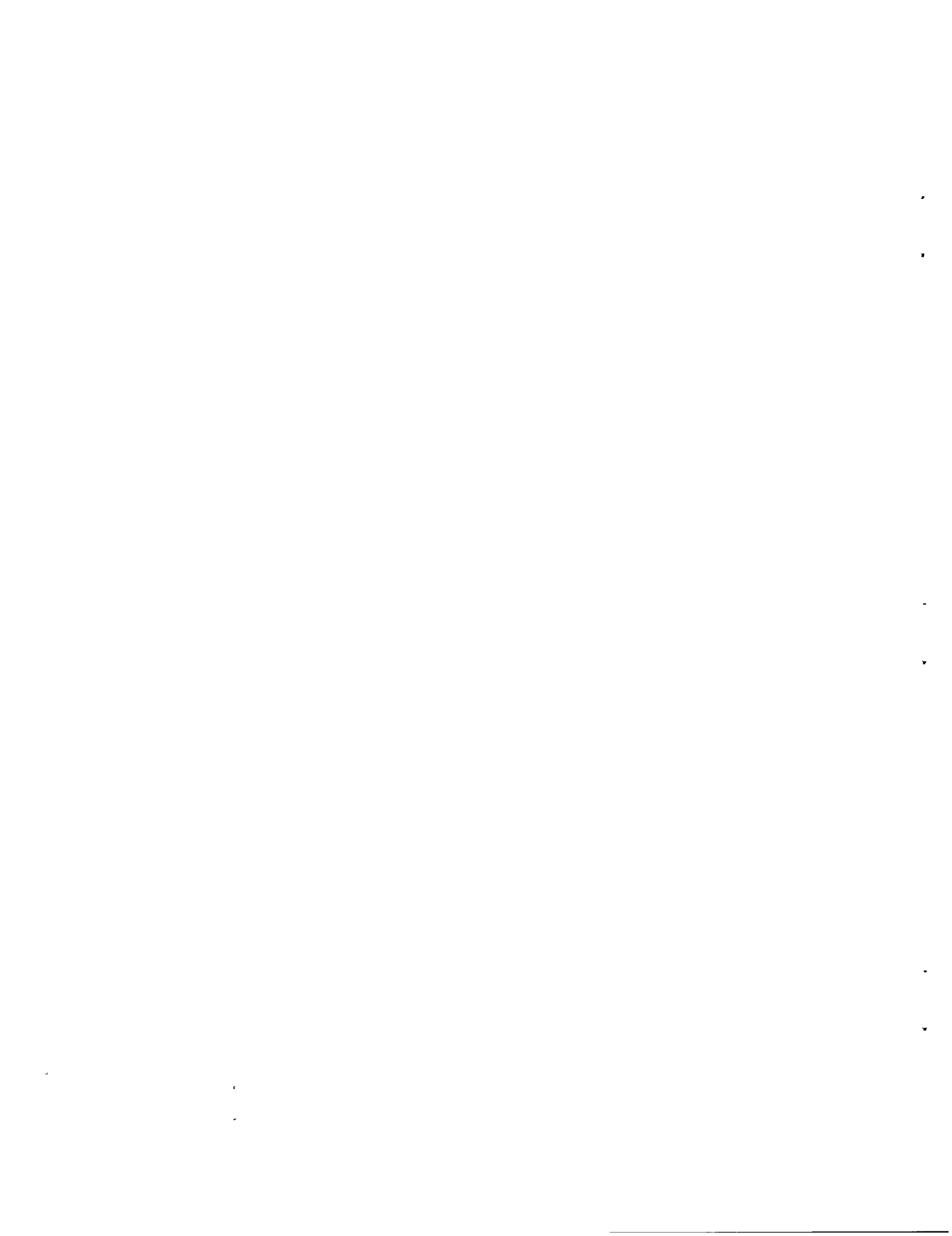
This report was prepared as an account of work sponsored by an agency of the United States Government. Neither the United States Government nor any agency thereof, nor any of their employees, makes any warranty, express or implied, or assumes any legal liability or responsibility for the accuracy, completeness, or usefulness of any information, apparatus, product, or process disclosed, or represents that its use would not infringe privately owned rights. Reference herein to any specific commercial product, process, or service by trade name, trademark, manufacturer, or otherwise, does not necessarily constitute or imply its endorsement, recommendation, or favoring by the United States Government or any agency thereof. The views and opinions of authors expressed herein do not necessarily state or reflect those of the United States Government or any agency thereof.

DISCLAIMER

This report was prepared as an account of work sponsored by an agency of the United States Government. Neither the United States Government nor any agency Thereof, nor any of their employees, makes any warranty, express or implied, or assumes any legal liability or responsibility for the accuracy, completeness, or usefulness of any information, apparatus, product, or process disclosed, or represents that its use would not infringe privately owned rights. Reference herein to any specific commercial product, process, or service by trade name, trademark, manufacturer, or otherwise does not necessarily constitute or imply its endorsement, recommendation, or favoring by the United States Government or any agency thereof. The views and opinions of authors expressed herein do not necessarily state or reflect those of the United States Government or any agency thereof.

DISCLAIMER

Portions of this document may be illegible in electronic image products. Images are produced from the best available original document.



CONTENTS

ABSTRACT	1
INTRODUCTION	1
EXPERIMENTAL PROCEDURE	3
MATERIALS	3
Welding	3
Microstructural Characterization	6
RESULTS AND DISCUSSION	6
MICROSTRUCTURE	6
EFFECT OF COOLING RATE ON THE MODE OF SOLIDIFICATION	22
IMPLICATIONS ON THE SCHAEFFLER DIAGRAM	30
CONCLUSIONS	39
ACKNOWLEDGMENT	40
REFERENCES	40

EFFECT OF RAPID SOLIDIFICATION ON STAINLESS STEEL
WELD METAL MICROSTRUCTURES AND ITS
IMPLICATIONS ON THE SCHAEFFLER DIAGRAM*

S. A. David, J. M. Vitek, R. W. Reed, and T. L. Hebble[‡]

ABSTRACT

An investigation was carried out to determine the effect of rapid solidification on the weld metal microstructure of austenitic stainless steels and its implication on the ferrite constitution diagram. A wide variety of stainless steels were laser welded at different welding speeds and laser power levels. The results indicate that both weld pool cooling rate and the postsolidification solid state cooling rates have a profound effect on the microstructures. For the steels investigated, the microstructures ranged from duplex austenite (γ) + ferrite (δ) to fully austenitic or fully ferritic. These microstructures were found to be sensitive to both cooling rates and composition. The observed results are rationalized based on rapid solidification theory.

Observations of this investigation indicate that solidification rates and postsolidification cooling rates have a profound effect on the observed microstructures, thus making it impossible to predict the microstructures of rapidly cooled weld metal from the conventional constitution diagrams. The influence of the observations made in this investigation on the Schaeffler diagram is demonstrated and possible corrections to the constitution diagram incorporating the cooling rate effects are proposed.

INTRODUCTION

Austenitic stainless steel is an extensively used engineering material for corrosion resistance and good low- and elevated-temperature mechanical properties. A significant problem in the production of fully austenitic stainless steel welds is their tendency toward hot cracking. To minimize this tendency, the compositions of weld filler metals are

*Research was sponsored by the Division of Materials Sciences, U.S. Department of Energy under contract DE-AC05-84OR21400 with Martin Marietta Energy Systems, Inc.

[‡]Computer Sciences Division.

generally modified to produce small amounts of delta (δ) ferrite in the as-welded microstructure. Such compositional changes promote the formation of ferrite as the primary solidification phase. Schaeffler¹ and DeLong² constitutional diagrams are successfully used to predict the ferrite content in austenitic stainless steel welds at room temperature. Also, a constitutional diagram has been developed for castings.³⁻⁵ These diagrams are all used to roughly estimate the ferrite level based on composition. The diagrams are based on the use of chromium equivalents (Cr_{eq}) and nickel equivalents (Ni_{eq}) which, with proper weighting factors, group together the ferrite forming elements such as chromium, silicon, and molybdenum and the austenite forming elements such as nickel, carbon, and manganese, respectively. However, these diagrams do not take into account the effect of weld metal solidification rate.

Rapid solidification of materials may produce microstructures during solidification that are markedly different from those observed during conventional solidification. During rapid solidification, the mode of solidification may change, the microstructural features are much finer, and solute segregation patterns may be greatly altered. During welding, which is one form of solidification processing, the cooling rates may vary from 10^2 to 10^6 °C/s, depending on the welding process. For conventional welding processes such as gas tungsten arc (GTA) and submerged arc (SA) cooling rates may be on the order of 10^3 °C/s. However, in the high power beam processes such as electron beam (EB) and laser welding, it is common to encounter cooling rates of the order of 10^4 to 10^6 °C/s.

It has been shown before that high cooling rates have altered the microstructures in stainless steel welds.⁶⁻⁸ Work on type 303 stainless steel has shown that extensive microstructural modification may occur during the rapid solidification of fine powders.⁹ Also, large degrees of undercooling have been shown to alter dramatically the structure of type 316 stainless steel.¹⁰ The purpose of this investigation is to characterize and understand the extent of modifications in microstructures that occur during rapid solidification of a wide variety of austenitic stainless steel welds. The work is also aimed at modifying the Schaeffler diagram to incorporate the microstructural changes observed as a function of weld metal cooling rates.

EXPERIMENTAL PROCEDURE

MATERIALS

The materials used in this investigation were commercial austenitic stainless steel weld filler metal alloys. The compositions of the alloys are given in Table 1. These alloys were selected to provide for different solidification modes. Two heats of all but one (alloy 446) of the alloys were evaluated to provide a range of compositions within the specifications for a given steel. The different heats will be distinguished by referring to each alloy with an "A" or "B" suffix. The ferrite forming tendencies of these alloys are reflected in their net chromium and nickel equivalents, calculated as¹

$$Cr_{eq} = Cr + Mo + 1.5 Si + 0.5 Nb ,$$

$$Ni_{eq} = Ni + 30 C + 0.5 Mn ,$$

where the symbols represent the elemental compositions in weight percent. The ratio of Cr_{eq}/Ni_{eq} for each alloy is also given in Table 1. The location of each alloy composition on the Schaeffler constitution diagram is shown in Fig. 1. As the Cr_{eq}/Ni_{eq} ratio increases the ferrite forming tendency of the alloy also increases.

Welding

Selected filler metal alloys were arc melted, drop cast into rectangular ingots and cold rolled down with intermediate annealing at 1050°C to 0.51-mm-thick sheets. Autogenous laser welds were made on 5 × 5 cm coupons using a pulsed Nd:YAG laser (Raytheon Model SS-500) capable of delivering an average power of 400 watts. A 6-in. focusing lens was used to focus the beam sharply onto the specimen surface. A pulse length of 1 ms and pulse rate of 200 pps were used in an argon atmosphere. In order to vary the heat input, and hence the cooling rate, two laser power levels 190-200 and 110-120 W were used. Welding speeds ranging from 12.7 to 254 cm/min were used.

Table 1. Compositions of the weld (wt %)

Steel Aisi-type	Cr	Ni	Mn	C	Si	P	S	Mo	Ti	Ta	Nb	Cr _{req}	Ni _{eq}	$\frac{Cr_{req}}{Ni_{eq}}$
304-A	18.85	9.54	1.38	0.05	0.51	0.023	0.019					19.62	11.73	1.67
304-B	18.16	8.63	1.28	0.06	0.72	0.032	0.007					19.24	11.07	1.74
308-A	20.12	9.72	1.78	0.04	0.38	0.023	0.005	0.06				20.75	11.81	1.76
308-B	19.17	10.57	1.92	0.06	0.72	0.045	0.016		0.56			20.25	13.33	1.52
309-A	23.84	12.75	1.80	0.05	0.39	0.024	0.008					24.43	15.15	1.61
309-B	23.01	13.41	2.08	0.02	0.46	0.011	0.003	0.01	0.11	0.01	0.01	23.72	15.05	1.58
316-A	17.01	11.50	1.86	0.04	0.30	0.016	0.012	2.30				19.76	13.63	1.45
316-B	19.25	12.73	2.22	0.03	0.45	0.042	0.018	2.34	0.39			22.27	14.74	1.51
312-A	28.92	8.44	1.24	0.13	0.43	0.018	0.004	0.15				29.72	12.96	2.29
312-B	29.72	8.78	1.68	0.11	0.39	0.025	0.005	0.20				30.51	12.92	2.36
347-A	19.5	10.0	1.50	0.06	0.60	0.018	0.020	0.10			0.70	20.85	12.55	1.66
347-B	19.38	8.66	1.21	0.04	0.35	0.010	0.019	0.05		0.01		19.96	10.47	1.91
446-A	26.62	0.34	1.15	0.14	0.45	0.022	0.016	0.10				27.40	5.12	5.36
310-A	26.73	21.15	1.64	0.11	0.50	0.014	0.009	0.05				27.53	25.27	1.09
310-B	25.62	19.18	0.90	0.03	0.42	0.013	0.005	0.15				26.40	20.53	1.29

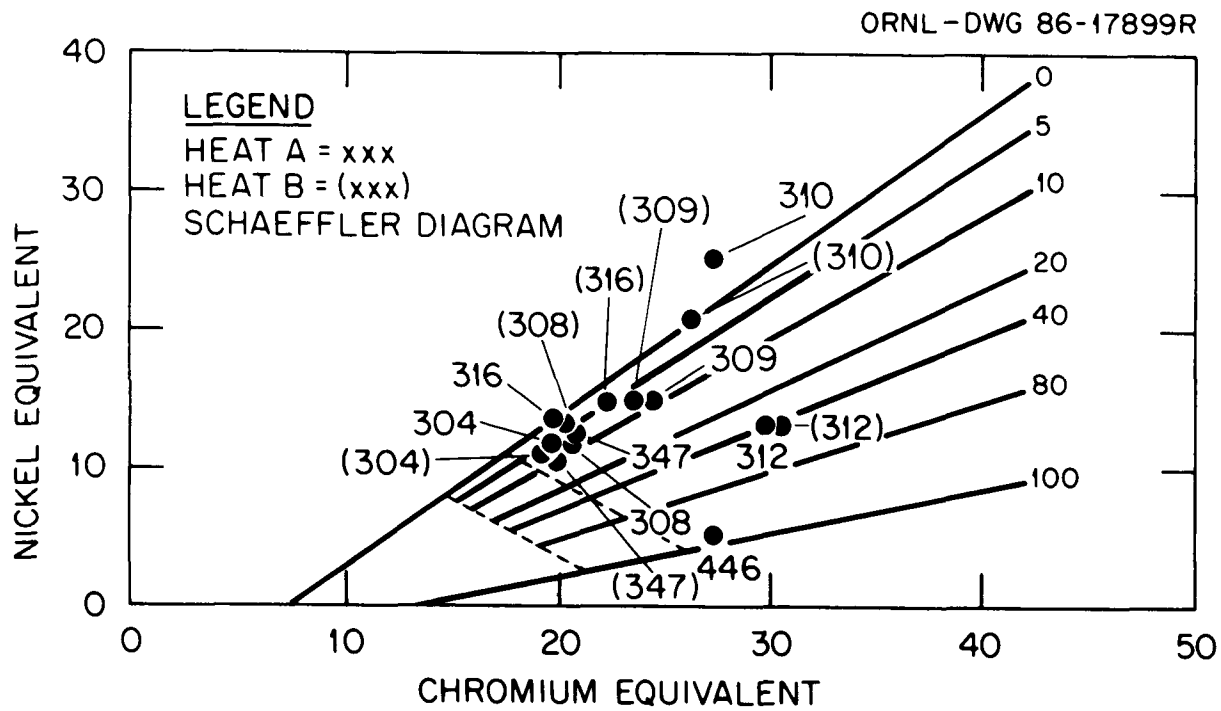


Fig. 1. Schaeffler diagram showing the location of the various steels selected for investigation on the diagram.

Microstructural Characterization

Microstructural characterization was done by optical as well as transmission electron microscopy. Metallographic specimens were etched using a solution containing HNO_3 and H_2O . The microstructures were examined by conventional light microscopy, paying special attention to the mode of solidification. Ferrite levels were evaluated optically by the point count method taking three independent measurements for each condition using a 10×10 grid. Electron microscopy was performed on thin foils with a JEOL 2000 FX electron microscope. The thin foils were taken from near the surface of the welds, in order to avoid any complications in specimens with only partial weld penetration. Thin foil specimens were made from wafers sliced from the welds and subsequently electrodischarge machined in to 3-mm-diam discs. The discs were then ground to a thickness of approximately 0.25 mm before being electrochemically polished. The foils were electropolished with a dual jet polishing apparatus and a solution of 10 vol % perchloric acid in methanol. The samples were polished at -10°C with 55 V dc. Phase identification was confirmed by electron diffraction.

RESULTS AND DISCUSSION

MICROSTRUCTURE

The as-welded microstructures were categorized by optical microscopy into one of three groups: fully austenitic, duplex austenitic and ferritic, and fully ferritic. In addition, in those alloys where ferrite was present, the amount of ferrite was determined by using a point counting method. Significant changes in the microstructures, compared to conventionally welded materials, were found for various combinations of laser welding conditions. The results on all heats for both power levels and all welding speeds are summarized in Table 2. Rather than consider each alloy and condition separately, the results will be grouped according to trends that were identified.

Table 2. Summary of microstructures

ORNL WSM 53664R

Laser Power Watts	Welding Speed cm/min	Estimated Cooling Rate $\times 10^6$ °C/sec	Series A								Series B						
			304 [1.67]	308 [1.76]	309 [1.61]	316 [1.45]	347 [1.66]	312 [2.29]	446 [5.36]	310 [1.09]	304 [1.74]	308 [1.52]	309 [1.58]	316 [1.51]	347 [1.91]	312 [2.36]	310 [1.29]
190-200	12.7	0.07	$\gamma+\delta$ (9.0)	$\gamma+\delta$ (13.5)	$\gamma+\delta$ (11.0)	$\gamma+\delta$ (15.0)	$\gamma+\delta$ (13.0)	$\gamma+\delta$ (80.0)	$\gamma+\delta$ (90.0)	γ	$\gamma+\delta$ (10.0)	$\gamma+\delta$ (12.0)	$\gamma+\delta$ (12.0)	$\gamma+\delta$ (19.0)	$\gamma+\delta$ (10.0)	$\gamma+\delta$ (90.0)	γ
	50.8	0.28	$\gamma+\delta$ (5.0)	$\gamma+\delta$ (13.0)	$\gamma+\delta$ (14.0)	γ	$\gamma+\delta$ (4.0)	$\gamma+\delta$ (90.0)	$\gamma+\delta$ (97.0)	γ	$\gamma+\delta$ (3.0)	$\gamma+\delta$ (2.0)	$\gamma+\delta$ (23.0)	$\gamma+\delta$ (23.0)	$\gamma+\delta$ (6.0)	$\gamma+\delta$ (88.0)	γ
	127.0	0.71	$\gamma+\delta$ (2.0)	$\gamma+\delta$ (15)	$\gamma+\delta$ (10.0)	γ	γ	δ	δ	γ	γ	γ	$\gamma+\delta$ (24.0)	$\gamma+\delta$ (21.0)	γ	$\gamma+\delta$ (90.0)	γ
	190.5	1.1	γ	γ	$\gamma+\delta$ (6.0)	γ	γ	δ	δ	γ	γ	γ	$\gamma+\delta$ (16.0)	$\gamma+\delta$ (16.0)	γ	δ	γ
	254.0	1.4	γ	γ	$\gamma+\delta$ (5.0)	γ	γ	δ	δ	γ	γ	γ	$\gamma+\delta$ (9.0)	$\gamma+\delta$ (6.0)	γ	δ	γ
110-120	12.7	0.12	$\gamma+\delta$ (10.5)	$\gamma+\delta$ (13.0)	$\gamma+\delta$ (15.0)	$\gamma+\delta$ (13.0)	$\gamma+\delta$ (14.0)	$\gamma+\delta$ (84.0)	$\gamma+\delta$ (90.0)	γ	$\gamma+\delta$ (13.0)	$\gamma+\delta$ (10.0)	$\gamma+\delta$ (14.0)	$\gamma+\delta$ (20.0)	$\gamma+\delta$ (18.0)	$\gamma+\delta$ (97.0)	γ
	50.8	0.47	$\gamma+\delta$ (9.0)	$\gamma+\delta$ (2.0)	$\gamma+\delta$ (19.0)	γ	$\gamma+\delta$ (2.0)	$\gamma+\delta$ (95.0)	$\gamma+\delta$ (98.0)	γ	$\gamma+\delta$ (3.0)	$\gamma+\delta$ (4.0)	$\gamma+\delta$ (21.0)	$\gamma+\delta$ (24.0)	$\gamma+\delta$ (10.0)	$\gamma+\delta$ (96.0)	γ
	127.0	1.2	γ	γ	$\gamma+\delta$ (18.0)	γ	γ	δ	δ	γ	γ	γ	$\gamma+\delta$ (10.0)	$\gamma+\delta$ (18.0)	γ	$\gamma+\delta$ (98.0)	γ
	190.5	1.8	γ	γ	$\gamma+\delta$ (8.0)	γ	γ	δ	δ	γ	γ	γ	$\gamma+\delta$ (3.0)	$\gamma+\delta$ (5.0)	γ	δ	γ
	254.0	2.3	γ	γ	$\gamma+\delta$ (3.5)	γ	γ	δ	δ	γ	γ	γ	$\gamma+\delta$ (1.0)	$\gamma+\delta$ (2.0)	γ	δ	γ

[] Cr_{eq}/Ni_{eq} ratio () Volume Pct ferrite

7

Most of the alloys (types 304, 308, 309, 312, 316, 347, and 446) consist of a duplex austenite plus ferrite microstructure following conventional welding. At the lowest laser welding speeds, these same duplex structures were observed. However, as the welding speed was increased, several different trends were noticed. For types 304A, 304B, 308A, 308B, 316A, 347A, and 347B, a decrease in the ferrite content was found as the welding speed increased. For these alloys, the decrease in ferrite content was gradual until a transition to a fully austenitic microstructure was noted. The welding speed at which the transition to a fully austenitic structure occurred varied according to the welding power level. For lower power levels, with correspondingly higher calculated cooling rates (Table 2), the transition typically took place at slower speeds. Furthermore, the transition often occurred at different welding speeds for different alloy heats. These effects are shown graphically in Fig. 2 for the 190 to 200 W power laser welds. The same trends were found for these alloys at the lower power level. A representative set of micrographs depicting this variation in ferrite content for alloy 308 is given in Fig. 3. Electron microscopy revealed the presence of an occasional grain of ferrite in the structures characterized as fully austenitic by optical microscopy (Fig. 4). However, the overall ferrite content in the nominally fully austenitic structures was well below 1%.

For several of the alloys in this group, no clear evidence of a solidification substructure in the fully austenitic condition was evident [Fig. 3(c)]. In contrast, for the type 316A alloy, a very well defined solidification microstructure was found by optical microscopy, as shown in Fig. 5(a). Electron microscopy of the fully austenitic types 308A and 316A welds indicated that the austenite grains were very fine. The dislocation densities for the two alloys were quite different with a low density in the former alloy (Fig. 4) and a high density in the latter [Fig. 5(b)]. These structures may suggest that possible recrystallization occurs during cooling subsequent to solidification and are the subject of further investigations.

A second group of alloys showed a different change in ferrite content with increasing cooling rate. For the alloys 309A, 309B, and 316B, a

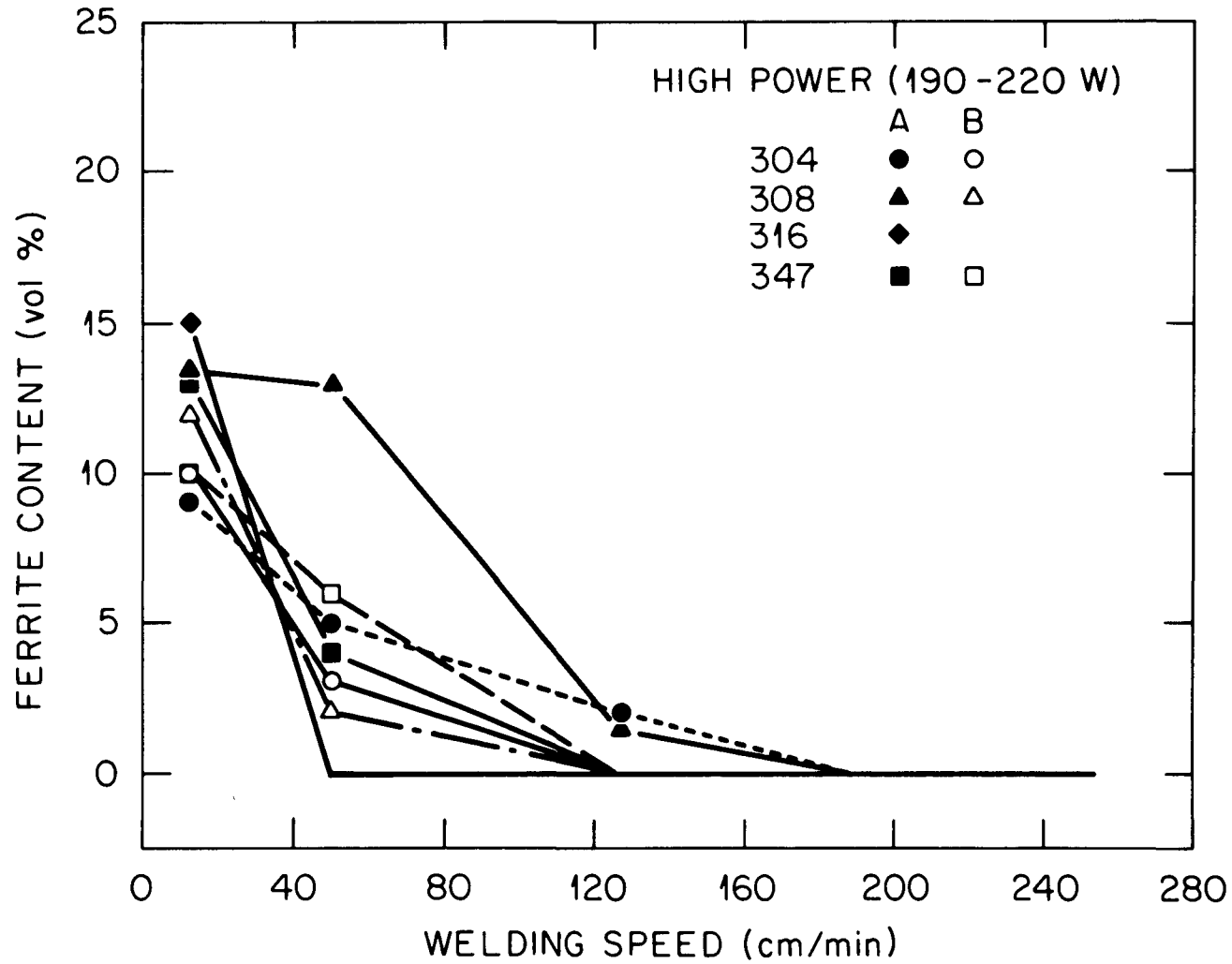


Fig. 2. Decrease in ferrite content as a function of welding speed observed for several steels (190 to 200 watt power level).

ORNL-PHOTO 1731-87

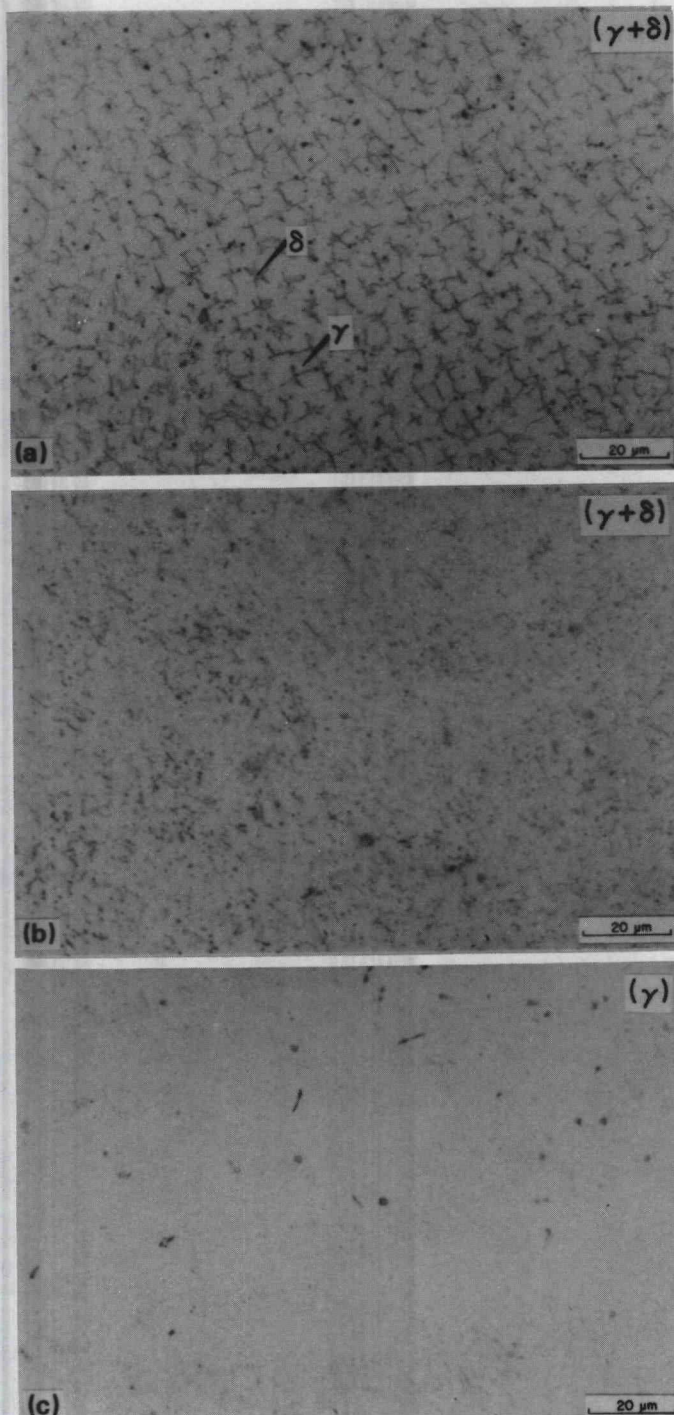


Fig. 3. Microstructures of type 308A laser welds (190 to 200 watt power) showing the transition to a fully austenitic structure with increasing welding speed. (a) 12.7 cm/min, (b) 50.8 cm/min, and (c) 190.5 cm/min.

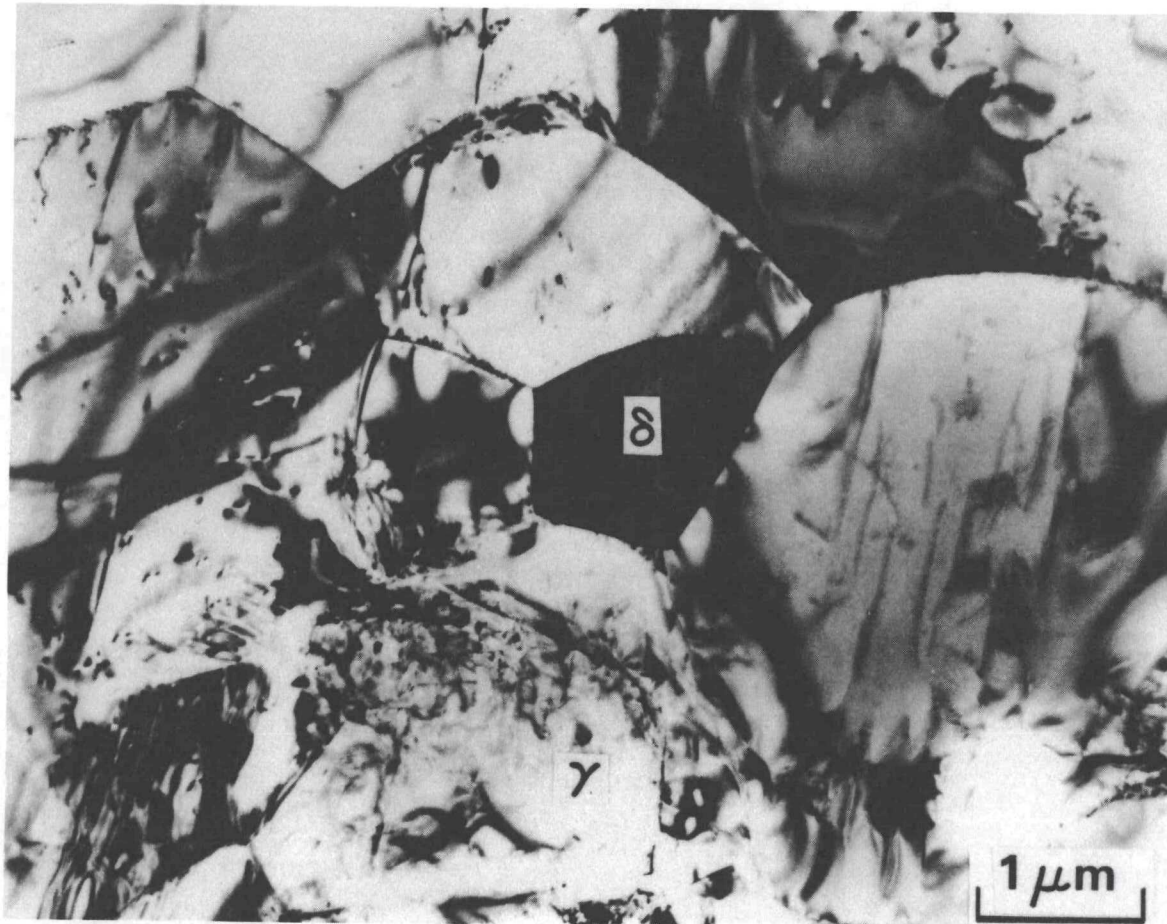


Fig. 4. TEM micrograph showing occasional ferrite and fine austenite grain size in the fusion zone of type 308B stainless steel laser welded at 12.7 cm/min (190 to 200 watt power level).

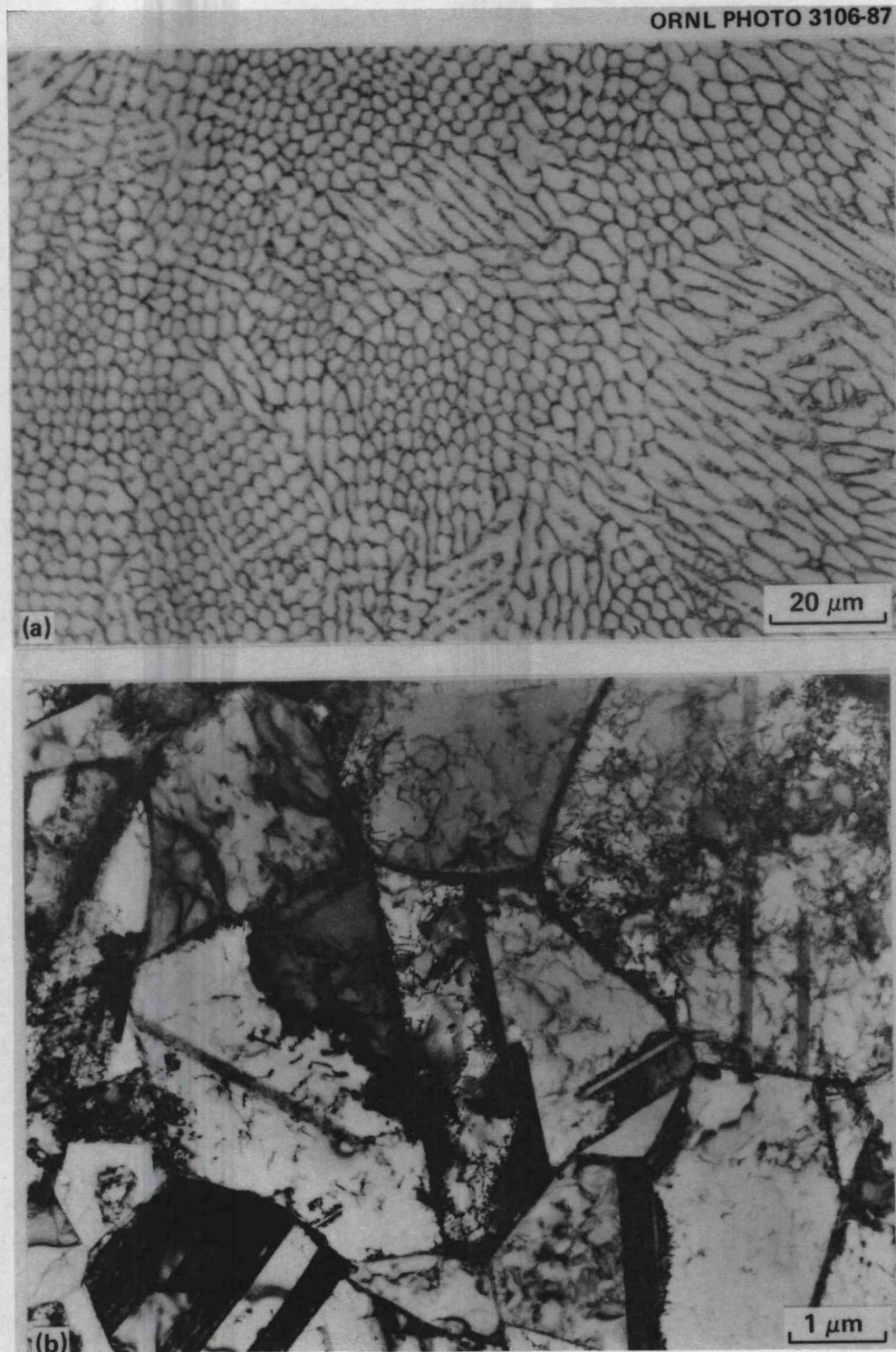


Fig. 5. Fully austenitic microstructure of type 316A stainless steel laser welded at 50.8 cm/min showing well-defined solidification structure and higher dislocation density. (a) Optical and (b) TEM micrographs.

transition to a fully austenitic microstructure was not found. In addition, as the cooling rate increased, the ferrite content initially increased before eventually decreasing. This behavior is shown in Fig. 6 for the 110 to 120 W power laser welds. Again, the same trends were found for these alloys at the other power level. A typical series of micrographs revealing the variation in ferrite level with welding speed (cooling rate) is shown in Fig. 7 for laser welded type 309A. There was a noticeable change in the ferrite morphology at the higher welding speeds. Whereas the ferrite morphology was vermicular at the lower welding speeds, the ferrite was distributed more randomly and was more disconnected in the materials welded at a higher speed [Fig. 7(a), (b) vs 7(c)]. Patchy areas of fully austenitic material were present, and these regions were found only at welding speeds beyond those corresponding to the maximum in the ferrite content vs welding speed curve (see Fig. 6).

Alloys 312A, 312B, and 446 showed yet another dependence of structure on welding speed. In these alloys, as the welding speed increased, the ferrite content also increased until a fully ferritic microstructure was obtained at the highest welding speeds. Under conventional welding conditions, 40 to 50% ferrite is typically present in the as-welded structure. However, under all of the laser welding conditions examined, significantly more ferrite was detected. A series of micrographs revealing this trend is shown in Fig. 8.

The fourth and final type of behavior with regard to ferrite variation with welding speed was found for alloy 310. Under conventional welding conditions, this alloy is fully austenitic. For all of the laser welding conditions tested, no change in the structure was found. The structure was fully austenitic, as revealed in Fig. 9. The microstructure was predominantly cellular dendritic with the size of the cells decreasing with increasing welding speed.

Significant variations in structure were often found among heats of the same alloy. This was particularly true for the type 309 and 316 steels. In the case of type 309, the same trend in ferrite content vs welding speed behavior was found for both heats, but the amount of ferrite was noticeably greater for the 309B heat. This may be due to the presence

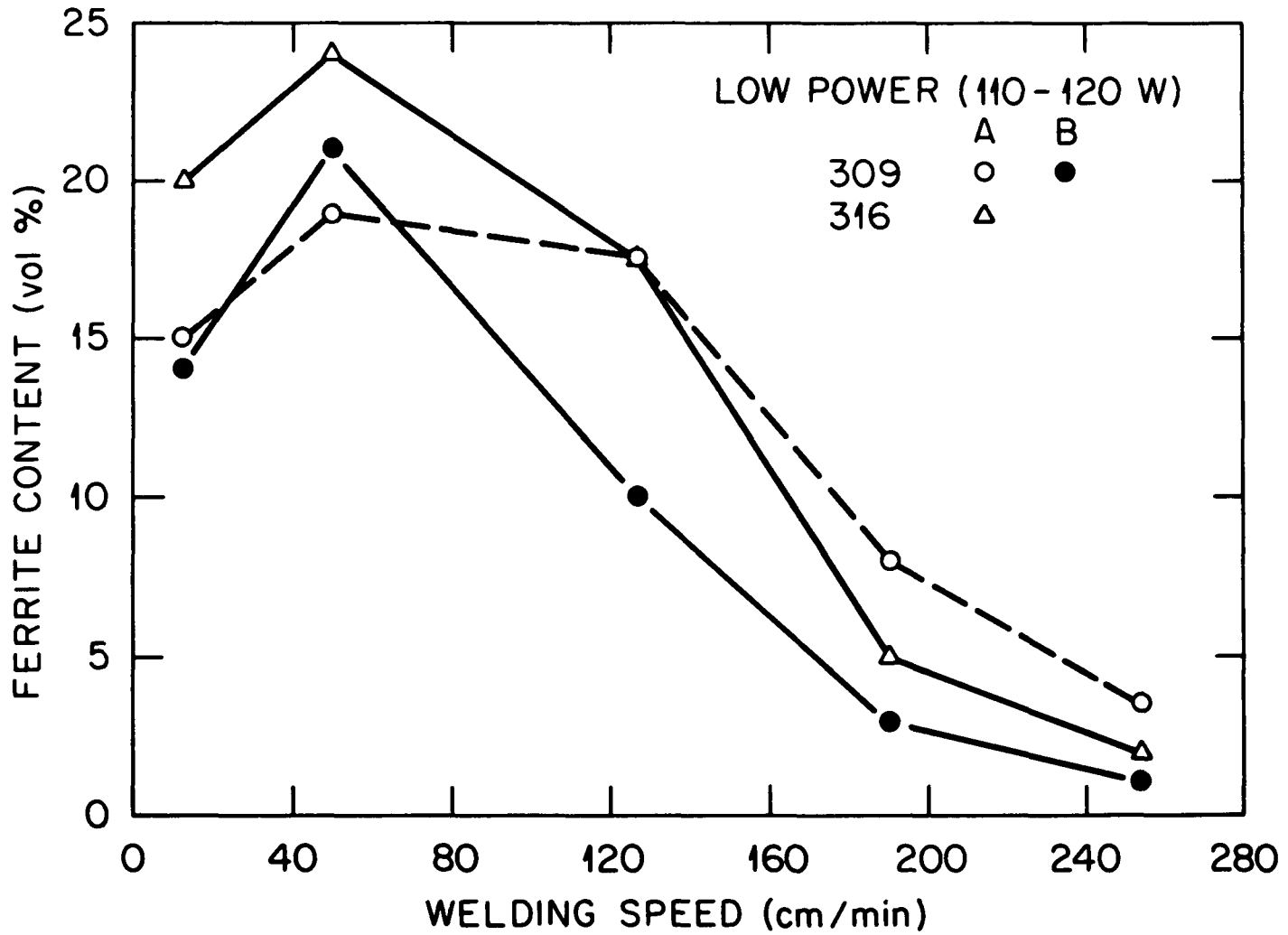


Fig. 6. Initial increase and subsequent decrease in ferrite content as a function of welding speed found for several steels (110 to 120 watt power level).

ORNL-PHOTO 1733-87

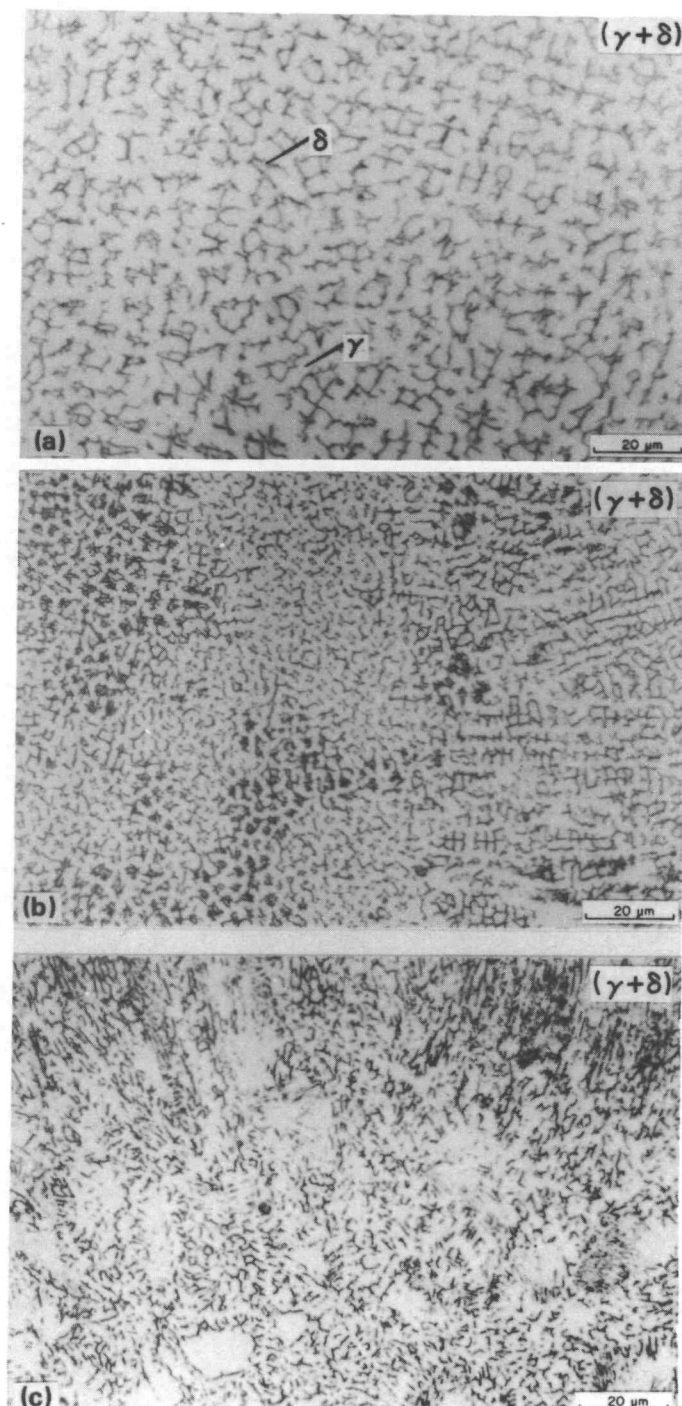


Fig. 7. Microstructures of type 309A laser welds (190 to 200 watts) showing initial increase and eventual decrease in ferrite number with increasing welding speed. (a) 12.7 cm/min, (b) 50.8 cm/min, and (c) 190.5 cm/min.

ORNL-PHOTO 1734-87

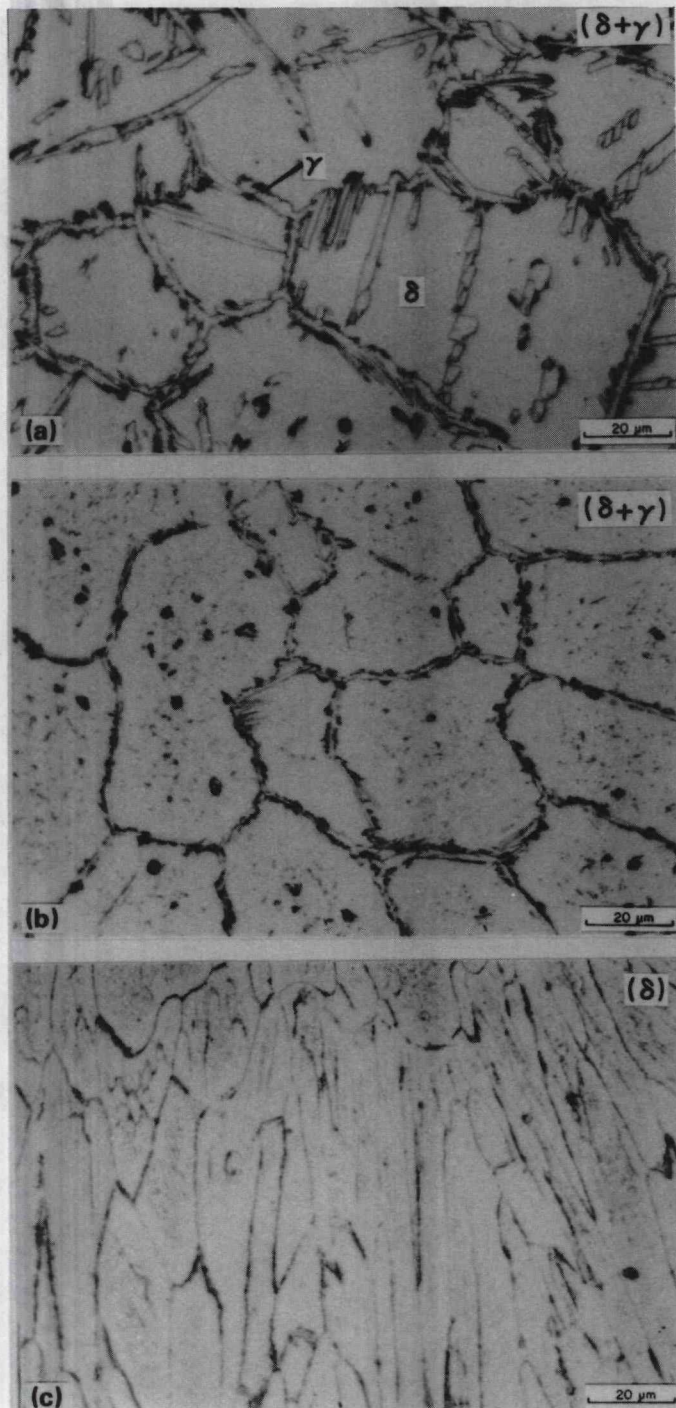


Fig. 8. Micrographs revealing the transition to a fully ferritic structure in type 312A laser welds as a function of welding speeds. (a) 12.7 cm/min, (b) 50.8 cm/min, and (c) 190.5 cm/min.

ORNL-PHOTO 1732-87

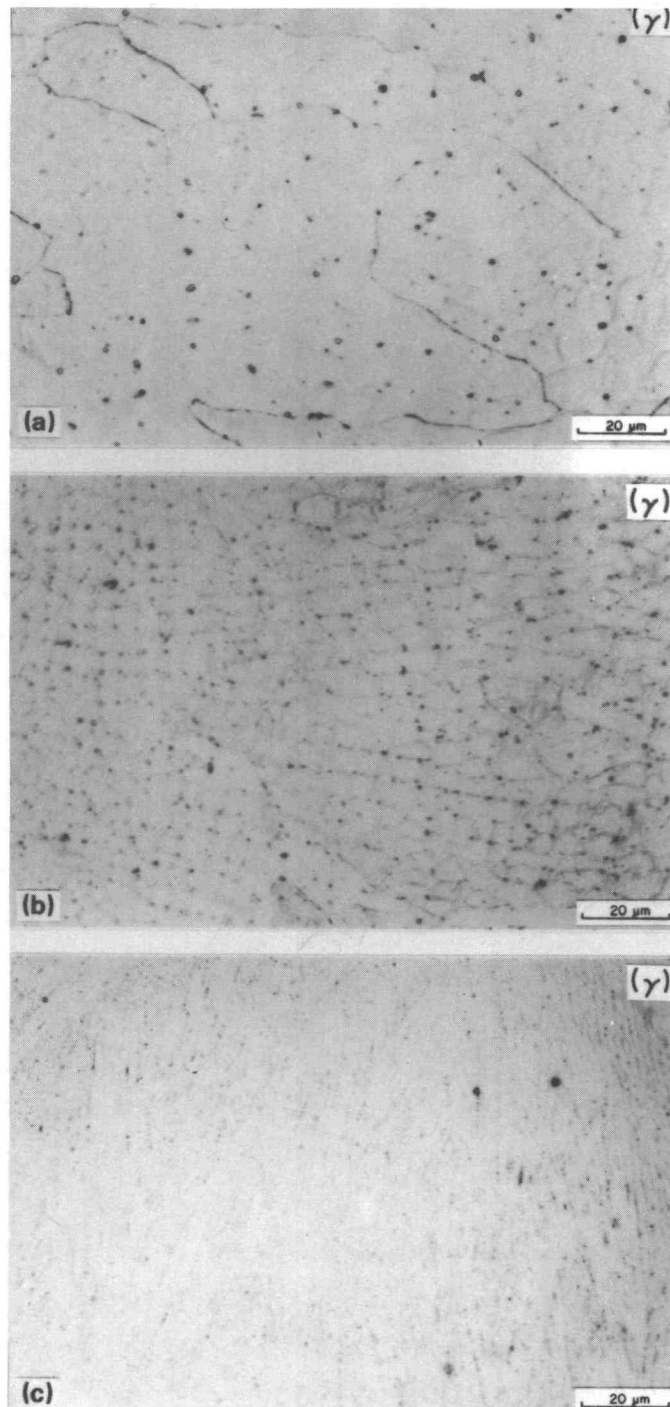


Fig. 9. Fully austenitic microstructures of type 310A laser welds found at all welding speeds. (a) 12.7 cm/min, (b) 50.8 cm/min, and (c) 190.5 cm/min.

of Ti, Ta, or Nb in the 309B heat, all of which are ferrite stabilizers. The difference between heats A and B of type 316 steel was even more dramatic. The ferrite content vs welding speed for these two heats is plotted in Fig. 10, and the microstructures are compared in Fig. 11. Whereas 316A showed a transition to a fully austenitic structure at higher welding speeds, no such transition was found for 316B. Thus, it is apparent that even if two heats remain within the compositional specifications of a given alloy, small changes in composition may lead to striking differences in the structures obtained after laser welding. The sensitivity to alloy composition will be discussed in more detail in the following sections.

Although a thorough analysis of hot cracking tendencies was not carried out, some important observations were made. Some cracks were found in the fully austenitic type 310 alloy. In contrast, no cracking was found in any of the other alloys, i.e., in either the duplex austenite plus ferrite structures, or in the fully austenitic structures, or the fully ferritic structures. Therefore, it is clear that a fully austenitic structure does not necessarily have to be prone to hot cracking. These results confirm earlier work^{6,7} in which cracking was also found in fully austenitic type 310 laser welds, but not in fully austenitic type 308 laser welds. The earlier work also showed some cracking tendencies in the fully ferritic type 312 laser welds. Such cracking was not found in this investigation. A more detailed examination of hot cracking behavior in rapidly solidified stainless steels is presently under way in our laboratory, and the results will be reported at a later date.

Finally, small, Mn, Si-rich, round inclusions were found in the laser welded structures. An example is shown in Fig. 12. Electron diffraction of these particles indicated they were amorphous in nature. Such amorphous MnSi particles had also been found in an earlier study.^{6,7} Recently Eagar¹¹ has shown that preferential evaporation may be a serious problem in welding. In fact, he indicated that manganese and silicon may be two species with a greater tendency toward evaporation during welding. Assuming this is the case for laser welding, it is hypothesized that the manganese and silicon vapors recondense on the wall of the keyhole formed

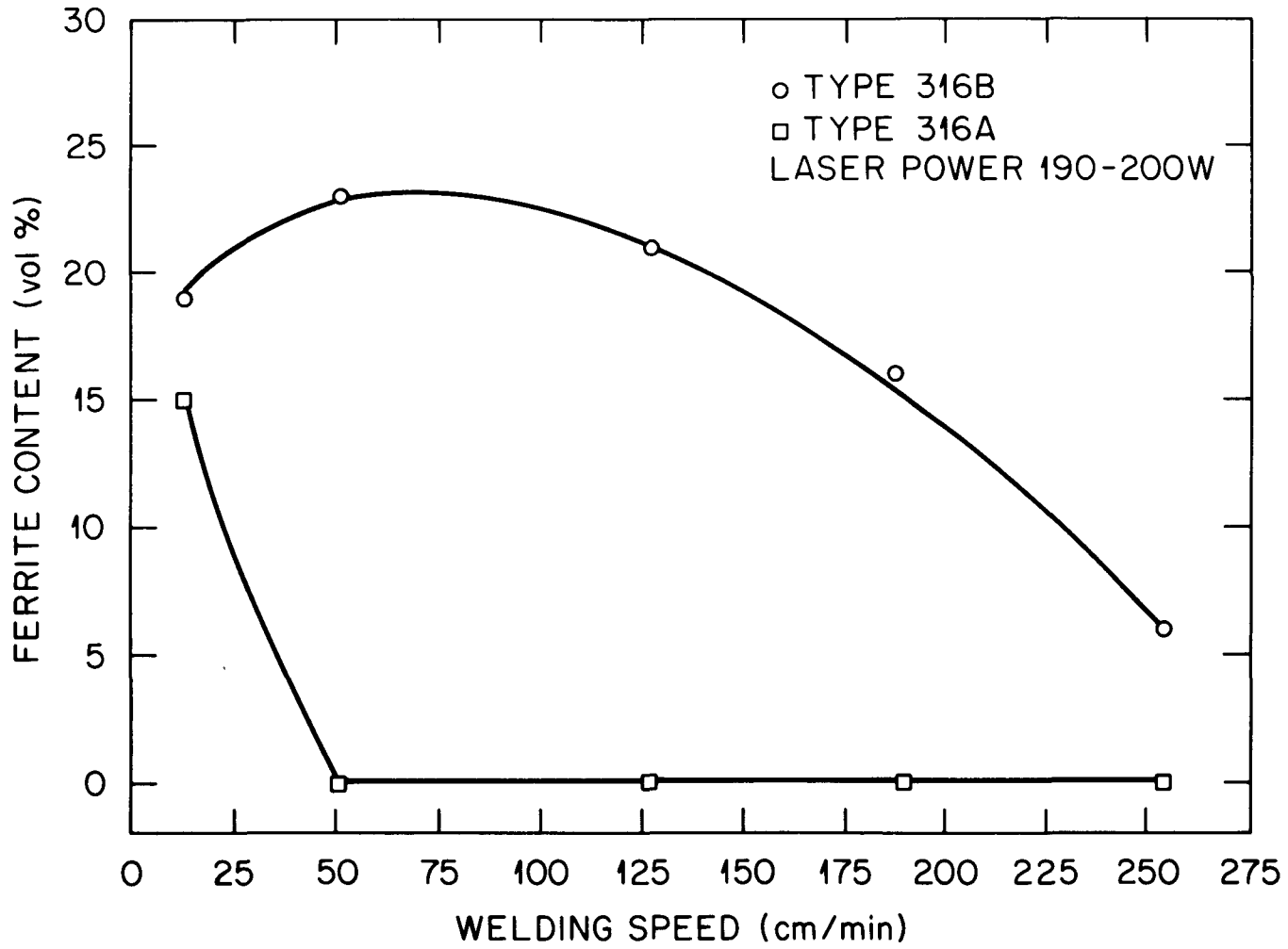


Fig. 10. Heat-to-heat variation of the dependence of ferrite content on welding speed for type 316A and 316B stainless steels.

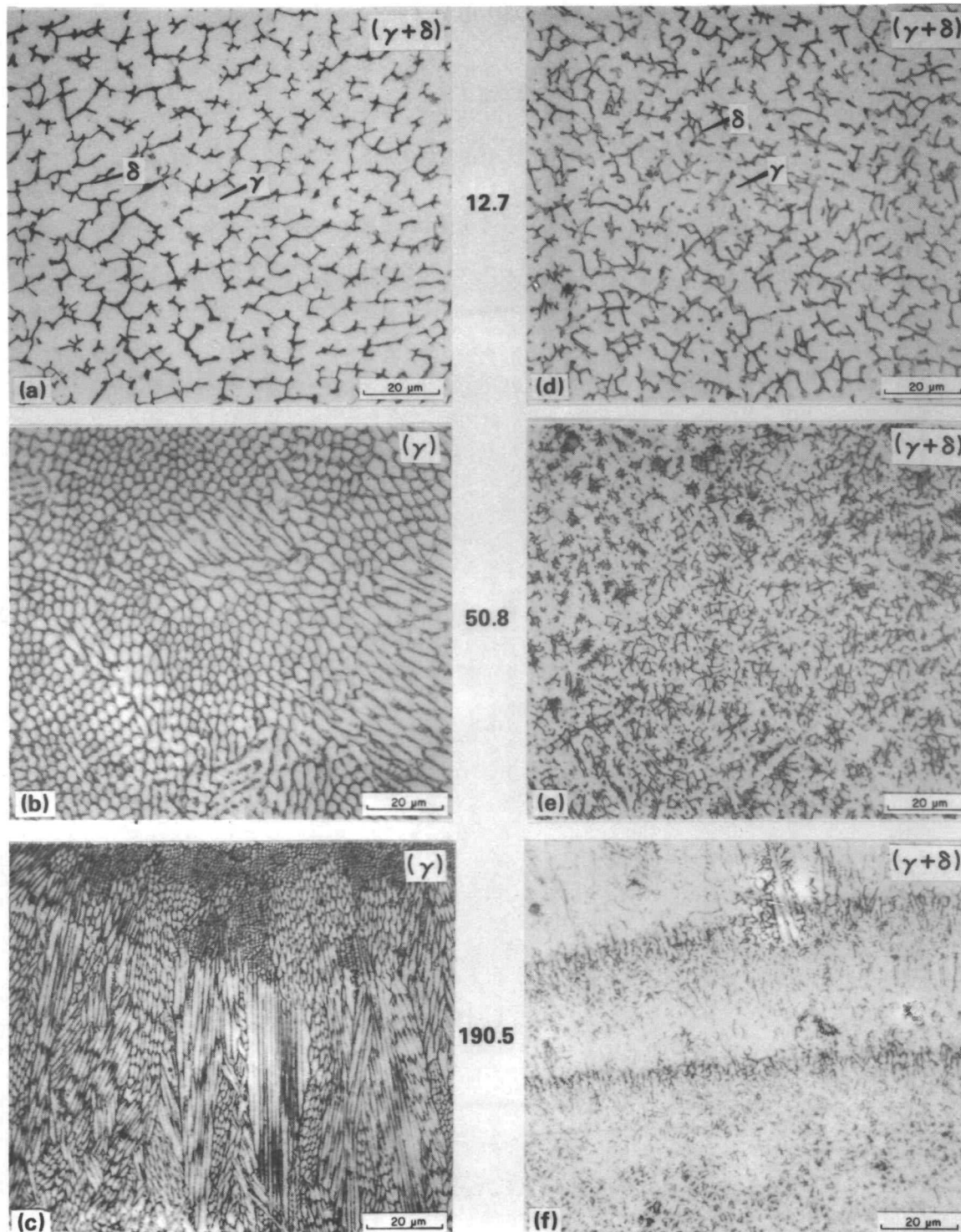


Fig. 11. Microstructures of type 316A laser welds at (a) 12.7 cm/min, (b) 50.8 cm/min, (c) 190.5 cm/min, type 316B laser welds at (d) 12.7 cm/min, (e) 50.8 cm/min, and (f) 190.5 cm/min.

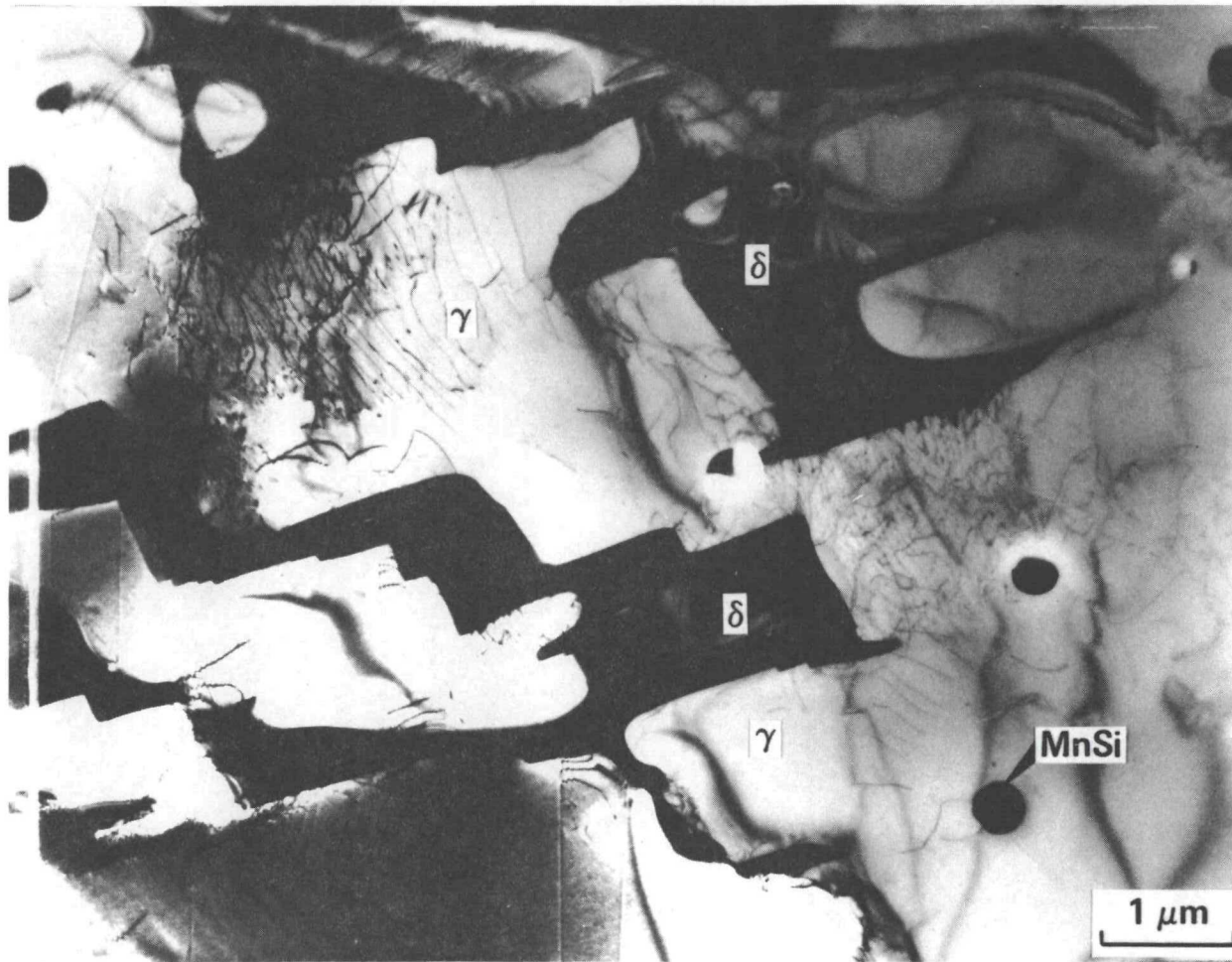


Fig. 12. TEM micrograph showing ferrite and amorphous MnSi particles in type 316A, laser welded at 12.7 cm/min.

during laser welding in the form of particles that are later incorporated into the structure. This mechanism explains the spherical shape of the particles.

EFFECT OF COOLING RATE ON THE MODE OF SOLIDIFICATION

An attempt was made to evaluate the cooling rates during solidification for the various laser welding conditions examined. Presently no rigorous model based on first principles of transport phenomena is generally available. Consequently, simple calculations were made using the approach of Adams¹² to provide a rough estimate of the cooling rates and to incorporate the effects of laser power and welding speed. Over the range of welding conditions investigated, penetration of the welds varied from full thickness to approximately quarter thickness. Therefore, the heat flow conditions varied from a 2D to 3D case; but the calculations were made using on the 3D case, which is appropriate for the higher cooling rate conditions. For the calculations, a laser absorptivity factor of 20% was used, based on the data in the literature.¹³ Based on the pulse rate and duration, the duty cycle was 20%. Cooling rates were calculated for a liquidus temperature of 1450°C for all alloys. The results of the cooling rate calculations are given in Table 2; and cooling rates covered the range from 0.07 to 2.3×10^6 °C/s.

Although the absolute values of the calculated cooling rates may not be very accurate, the purpose of these calculations was to examine the trends between the cooling rate and the laser speed, power, and microstructure. Such trends predicted by the Adams mode should be reliable. Comparing the calculations to other estimates of cooling rates, the present calculations to other estimates of cooling rates, the present calculations appear to be accurate to within an order of magnitude. The microstructures produced by laser welding for the higher cooling rates are similar to those found in splat quenched specimens,⁷ for which the cooling rates have been estimated¹⁴ to be at least 10^6 °C/s. Others have estimated¹⁵ the cooling rates for laser welding to be on the order of 10^5 to 10^6 °C/s, again in agreement with our approximate calculations. Finally, in one specimen the secondary dendrite areas were discernable and

the area spacings could be approximated. The spacings can be related to cooling the rates.⁸ For a measured secondary dendrite area spacings of 0.7 μm in a type 310 stainless steel specimen welded at 254 cm/min with a laser power of 200 watts, a corresponding cooling rate of 7×10^5 $^{\circ}\text{C/s}$ was found, in reasonable agreement with the calculated value of 1.4×10^6 $^{\circ}\text{C/s}$ encountered during laser welding result in rapid solidification conditions. Furthermore, the relative changes in cooling rates for the two power levels and for the five welding speeds involved are probably much more reliable. Thus, the cooling rates for the lower welding power are expected to be 67% greater at comparable welding speeds. Equivalently, the cooling rates achieved at the lower power levels are equal to the rates at the higher power level if the welding speeds are 67% faster.

Four types of solidification modes can be identified for the stainless steels under consideration.¹⁶ These are ferritic (F), ferritic-austenitic (FA), austenitic-ferritic (AF), and austenitic (A). Briefly, these modes may be described as follows: F - primary ferrite solidification only; FA - primary ferrite solidification with austenite solidification at the later stages as a result of a peritectic reaction; AF - primary austenite solidification with some ferrite solidification as a result of solute segregation; A - primary austenite solidification only. A more complete description may be found in ref. 16. The mode of solidification expected for each of the alloys under conventional welding conditions is given in Table 3. Most of the alloys evaluated solidify in either the F or FA modes during conventional welding processes. For these solidification modes, as the weld is cooled from elevated temperatures the ferrite becomes unstable and undergoes a solid-state transformation to austenite.¹⁷ Since the cooling rates even under conventional welding conditions are relatively high ($>10^2$ $^{\circ}\text{C/s}$), the solid-state transformation of ferrite to austenite is normally not completed and some residual ferrite remains in the as-welded structure. If the cooling rates are increased substantially, as in the case of laser welding, then one might expect this solid-state transformation to be retarded, or even suppressed completely. This is precisely what happens for the types 312 and 446 alloys. The amount of residual ferrite present in the as-welded condition is significantly greater for laser welds than the typical ferrite content of 40 to

Table 3. Modes of solidification

Alloy	Solidification mode ^a	Cr _{eq} /Ni _{eq}
304A	FA	1.67
304B	FA	1.74
308A	FA	1.76
308B	FA	1.52
309A	FA	1.61
309B	FA	1.58
316A	FA (AF) ^b	1.45
316B	FA (AF) ^b	1.51
312A	F	2.29
312B	F	2.36
347A	FA	1.66
347B	FA	1.91
446	F	5.36
310A	A	1.09
310B	A	1.29

^aA = single phase austenitic; AF = austenitic-ferritic; FA = ferritic-austenitic; F = single phase ferritic.

^bGenerally shows a mixed mode of freezing, FA-AF.

50% found in conventionally welded materials. Furthermore, with higher cooling rates, the ferrite to austenite solid-state reaction is suppressed completely, yielding a fully ferritic microstructure.

The increase in the ferrite content with increasing cooling rate is also found at the lower welding speeds for alloys 309A, 309B, and 316B. However, as the welding speed is increased even further, this trend is reversed (see Fig. 6). This decrease in ferrite content with increasing cooling rates, observed at the higher cooling rates, cannot be explained by assuming the solid-state transformation is simply retarded at the higher cooling rates. A decrease in the ferrite content with increasing cooling rate is observed for several other alloys (types 304, 308, 347, and 316 heat A) at all welding speeds. In this latter group, the ferrite level eventually decreases to zero beyond some critical cooling

rate, the value of which is both alloy and heat dependent. The fully austenitic weld metal structures observed in this latter group of steels must be due to a change in the mode of solidification to one of primary austenite formation (A mode). For intermediate cooling rates which are insufficient to produce a fully austenitic structure, one of two possibilities may occur. Due to segregation during solidification, some ferrite may form in the intercellular regions, resulting in an AF mode of solidification. Some evidence of such a sequence can be seen in Fig. 3(c) and Fig. 4, where very small quantities of intercellular ferrite can be identified. Alternatively, a mixed mode of solidification may occur, with a combination of either AF + FA, or A + FA. Such a structure would consist of patches corresponding to the different solidification modes. The disconnected ferrite morphology shown in Fig. 7(c) may be caused by such a mixed mode of solidification. More striking evidence for a mixed mode of solidification is shown in Fig. 13, where very distinct patches of fully austenitic regions are clearly visible within a duplex austenite plus ferrite matrix. Mixed mode solidification in type 316 steel has also been identified previously.¹⁸ These alternative solidification mechanisms can readily explain the gradual decrease in ferrite content with increasing cooling rate found for cooling rates below the critical cooling rate necessary to produce a fully austenitic structure.

The behavior of types 309A, 309B, and 316B steels is atypical in that a fully austenitic structure is not found over the entire range of cooling rates evaluated. This is simply an indication that the critical cooling rate necessary to solidify these alloys entirely in the primary austenite mode was not achieved under the conditions tested. The results support this idea. First, the fact that the ferrite content decreases with increasing cooling rate at the higher cooling rates demonstrates that the critical cooling rate is being approached. Second, Fig. 13 clearly shows fully austenitic regions, again indicating that the cooling rate is very close to the critical rate needed for a fully austenitic structure. Furthermore, Fig. 13 shows that the volume percent of fully austenitic regions increase with increasing welding speed. It is noteworthy that a

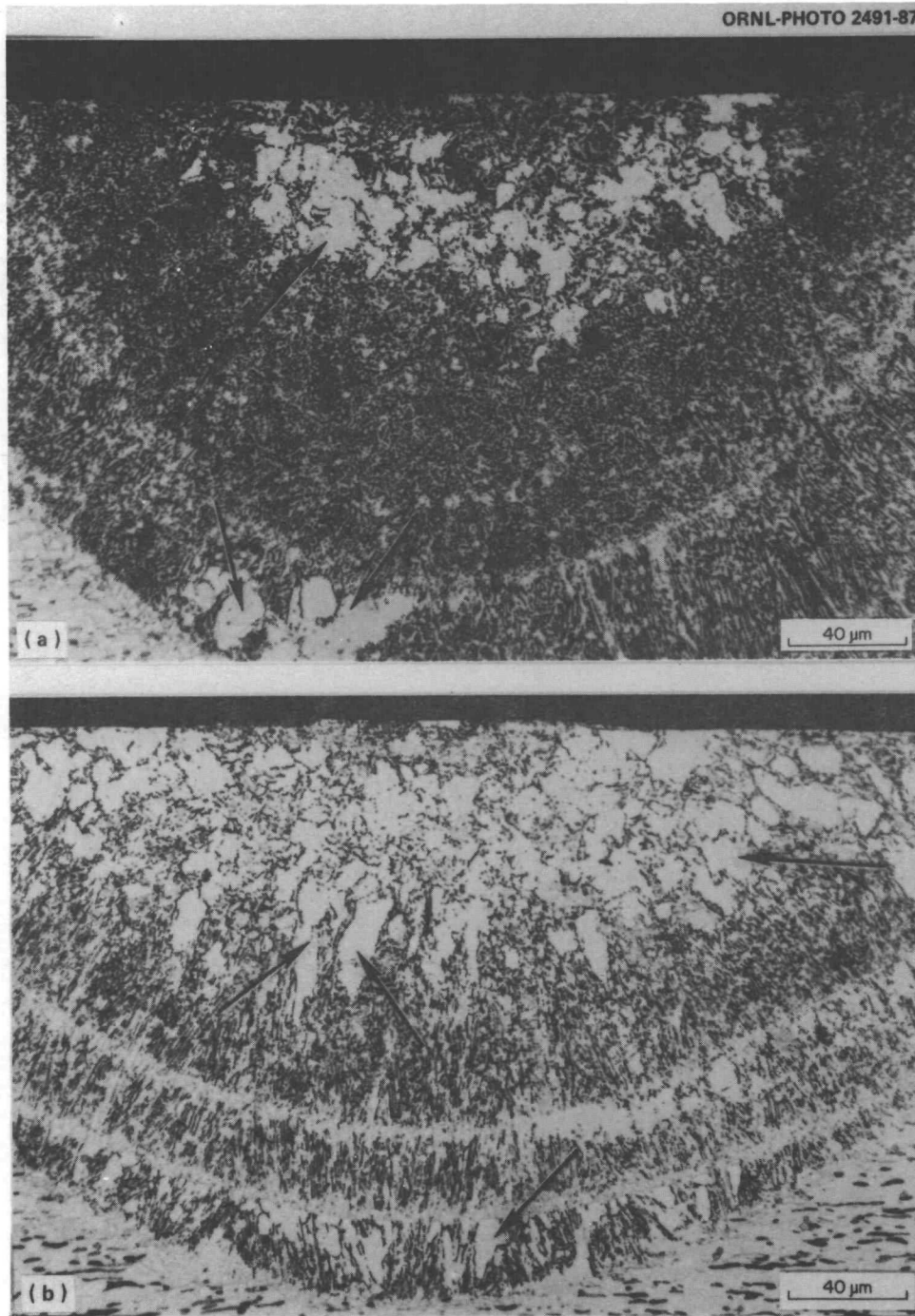


Fig. 13. Microstructures of type 309B laser welds showing fully austenitic regions that increase in volume percent with increasing welding speed. (a) 127 cm/min and (b) 190.5 cm/min.

fully austenitic structure was produced in alloy 316A at relatively low cooling rates, indicating a very sensitive dependence of the critical cooling rate on composition.

The competition between primary austenite formation and primary ferrite formation, and the effect that solidification rate may have, can be readily understood by referring to a schematic vertical section of the Fe-Cr-Ni phase diagram. Such a section is shown in Fig. 14, with lines approximately representing three austenitic steel composition superimposed. The T_0 lines¹⁹ representing partitionless solidification of either austenite or ferrite have also been sketched. The T_0 lines represent the loci of temperatures below which the single phase austenite (or ferrite) has a lower free energy than the single phase undercooled liquid. The T_0 lines must lie within the (L + γ) or the (L + δ) phase fields and they have been schematically extended to cover a wider range of alloy compositions.

For alloys that normally solidify in the F mode, such as the type 312 steel, undercooling during laser welding may be sufficient to bring the liquid below the ferrite T_0 line. Thus, the only solidification mode available upon cooling is the F mode. On the other side of the diagram, alloys that normally solidify in the A mode such as 310 continue to solidify in this mode because the undercooling during rapid solidification is likely to be great enough to bring the liquid below the austenite T_0 line, but not below the ferrite T_0 line. Therefore, only partitionless austenite formation is possible. For intermediate compositions, such as those for types 308, 304, 309, 347, and 316 steels, the undercooling achieved during rapid solidification may be sufficient to bring the liquid below the T_0 lines of both austenite and ferrite.²⁰ If this occurs, the actual mode of solidification will depend on the relative kinetics of nucleation for austenite and ferrite. Kelly et al.⁹ have addressed the issue of the relative nucleation rates for austenite and ferrite. They have found that in the presence of heterogeneous nucleation sites, which are readily available in larger solidification volumes such as those in the present study, austenitic solidification is kinetically favored. Although their analysis was for type 303 stainless steel, it is possible that the same conclusions may be applicable to austenitic stainless steels in general.

ORNL-DWG 82-20422R

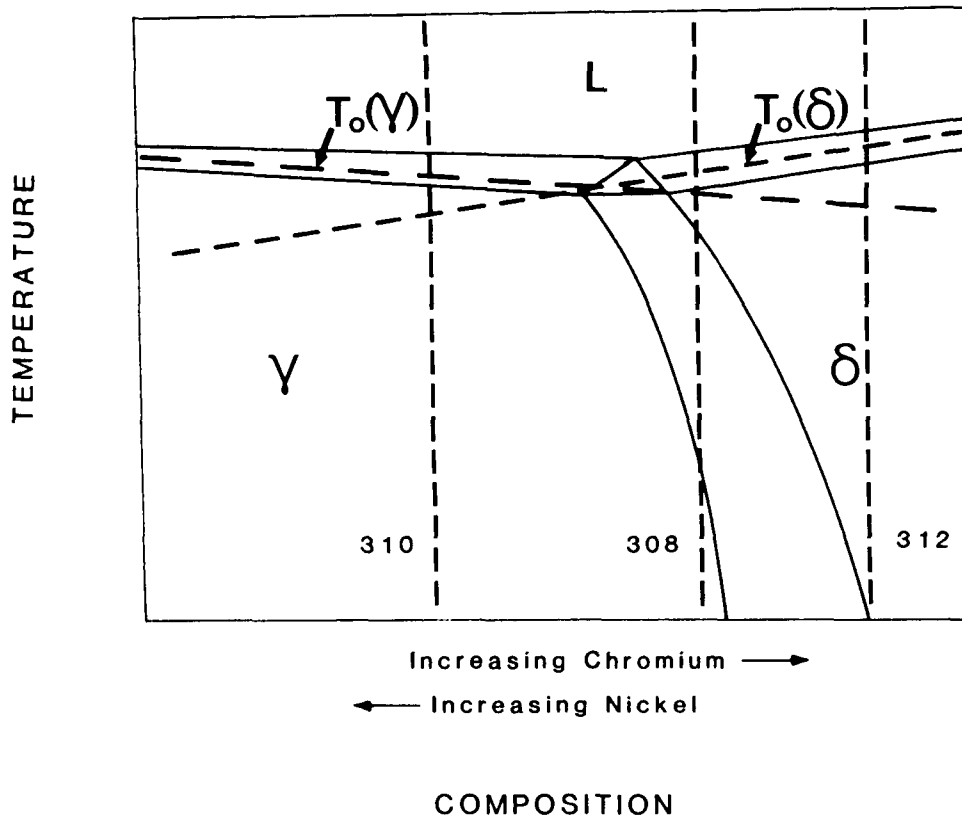


Fig. 14. Schematic diagram of a vertical section of the Fe-Cr-Ni phase diagram, with schematic T_0 lines for partitionless ferrite or austenite solidification superimposed. Approximate compositions of three alloys are qualitatively indicated for discussion purposes.

Therefore, if a critical undercooling is achieved such that the liquid is brought below the T_0 lines for both austenite and ferrite, the austenite solidification will be dominant because of the faster kinetics for this reaction. Thus, for the alloys 304, 308, 347, and 316A, the laser welding conditions were presumably sufficient to undercool the liquid below the austenite T_0 line, resulting in a change in the solidification mode to that of primary austenite formation. Apparently such a critical undercooling was not achieved in the case of the 309 and 316B steels.

The interpretation of the results has been based on the assumption that, when possible, partitionless solidification will occur. However, some solute partitioning has been observed by analytical electron microscopy, and can be inferred from the presence of intercellular ferritic areas such as those in Figs. 3 and 4. The degree of partitioning is expected to be a function of the laser welding speed. However, the presence of a small amount of partitioning should not influence, in any major way, the conclusions that were drawn. The concept of partitionless solidification is still a simple and useful way of understanding the observed behavior, and the small degree of partitioning present in the rapidly cooled laser welds can be considered as a small perturbation on these conclusions.

A change in the mode of solidification with cooling rate has been observed to a limited extent before. Earlier work on three stainless steels showed that both laser welding as well as splat quenching can change the mode of solidification from that of primary ferrite to one of primary austenite formation.⁷ It was found that a change in solidification mode was very sensitive to cooling rate for rates on the order of 10^6 °C/s, comparable to the cooling rates calculated for the laser welding conditions in this study. Within a splat quenched foil in which no detectable change in composition through the thickness was measured, a change in the mode of solidification was found between the surface of the foil and the slightly slower cooled foil interior. In addition, a change in solidification mode was found between the root and crown of a single autogenous laser weld. Such a sensitivity to cooling rate agrees with the findings in the present study. Suutala²¹ also found some evidence for a

change in the mode of solidification in gas tungsten arc (GTA) welds. He observed that at higher solidification rates the mode changed from one of primary ferrite to that of a mixed primary ferrite and primary austenite. Presumably the cooling rates prevalent during GTA welding were insufficient to obtain a fully austenitic structure. Suutala concluded that under the welding conditions he employed, cooling rates played only a minor, secondary role to that of composition in determining the mode of solidification. Lippold,²² on the other hand, found a change in the solidification mode from primary ferrite to primary austenite that resulted in a fully austenitic structure at the weld centerline of electron beam welds of type 304L stainless steel. He associated the presence of a fully austenitic structure with the areas subjected to the highest solidification rates, in agreement with the findings in the present and earlier studies.^{6,7}

IMPLICATIONS ON THE SCHAEFFLER DIAGRAM

Since it is clear from the observations that cooling rate plays a major role in determining the solidification mode and the final microstructure of rapidly solidified welds, an attempt has been made to incorporate the results of this study into the Schaeffler diagram by adding cooling rate as a new dimension. In the Schaeffler diagram, each of the limited number of constant ferrite content contour lines may be described by the following relation:

$$(Ni_{eq} - Ni_0) = S (Cr_{eq} - Cr_0) , \quad (1)$$

where

Ni_{eq} and Cr_{eq} = the nickel and chromium equivalents defined for the Schaeffler diagram,

S = the slope of the contour line,

Ni_0 and Cr_0 = the nickel and chromium equivalent composition coordinates of the intersection of the 0 and 100% ferrite contour lines.

The intersection of the contour lines $[(4.95, -2.53)]$ was determined from point and slopes estimates extracted from the Schaeffler diagram. The slope and intercept for each contour are listed in Table 4. Using the data in Table 4, a third order polynomial was found to represent adequately the slope of any contour as a function of ferrite content at low cooling rates appropriate for the Schaeffler diagram.

Table 4. Parameter estimates for ferrite contours in Schaeffler diagram

Contour, % Ferrite	Slope	N _{ieq} Intercept
0.0	1.09	-8.0
5.0	1.00	-7.5
10.0	0.88	-6.9
20.0	0.73	-6.2
40.0	0.64	-5.7
80.0	0.50	-5.0
100.0	0.32	-3.9

The effect of cooling rate was introduced by considering only the 0 and 100% ferrite contours and allowing these contours to change with increasing cooling rate. The intersection of these two contours was kept constant at the same point as in the original Schaeffler diagram, and the contours were also assumed to remain straight lines. As the cooling rate increases, the 0 and 100% contours were allowed to change to the positions of the contour lines corresponding to F and F' percent ferrite respectively in the original Schaeffler diagram. The procedure for incorporating the effect of cooling rate is quite simple; available data do not warrant the use of a more complicated model. The expressions for the 0 and 100% ferrite contours in terms of F and F' are, respectively,

$$F = 8.5 R_c, \text{ and} \quad (2)$$

$$F' = 100 - 25 R_c, \quad (3)$$

where F and F' represent the corresponding contour lines for the percent ferrite in the original Schaeffler diagram and R_c is the cooling rate ($^{\circ}\text{C/s}$) $\times 10^{-6}$ ($0.01 < R_c < 2.3$). These equations represent a fit for all of the 15 alloy compositions and 10 cooling rates investigated. It should be remembered that these equations are limited by the accuracy of the estimated cooling rates.

From plots of the data at different levels of cooling rate, the slopes of the 0 and 100% ferrite contours tended to approach the slope of the 30% contour in the original diagram as cooling rate increased. Thus, the slope of the limiting contour was defined to be the slope of the 30% ferrite contour. At a cooling rate of 9.1×10^6 $^{\circ}\text{C/min}$, the 0% contour took on the original slope of the 20% contour in the Schaeffler diagram and the 100% contour took on the slope of the 40% line.

The modified Schaeffler diagrams for all of the higher cooling rates are presented in Fig. 15. At the lowest cooling rate considered (0.07×10^6 $^{\circ}\text{C/s}$), Fig. 15(a), there is very little change in the location of the contour lines compared to the positions in the original diagram (Fig. 1). This is a reflection of the fact that at the lower cooling rates evaluated in this study, the structures were comparable to those found under conventional welding conditions. This also agrees with the conclusion of others²¹ that at low cooling rates the structure is very weakly dependent on cooling rate. However, as the cooling rate increases, it is evident that the two contour lines must converge in order to fit with the experimental results. This is shown in Fig. 15(b) through 15(j). Compositions that were within the two phase field in the original diagram now may lie outside the two contour lines, indicating that the structures are no longer duplex austenite plus ferrite, but rather single phase austenite or single phase ferrite. A composite diagram showing cooling rate as a third dimension for the constitution diagram for welds is shown in Fig. 16.

Some discrepancies do exist. For example, at the highest cooling rate [Fig. 15(j)], it was not possible to include the three alloys 309A, 309B, and 316B into the two phase region, where they belong, without

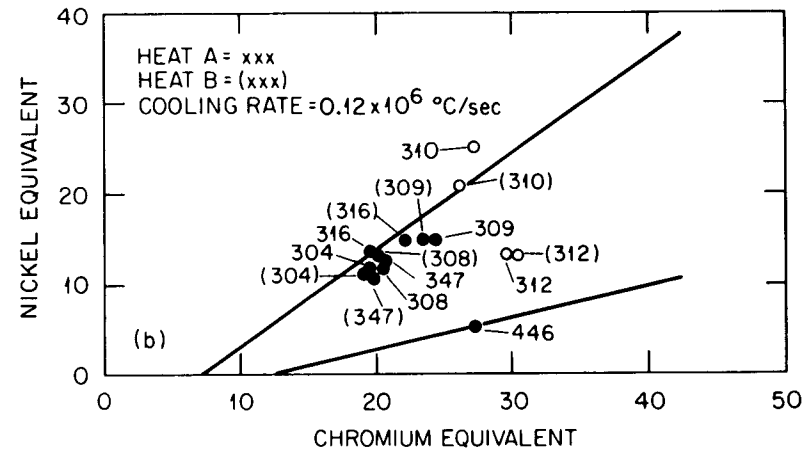
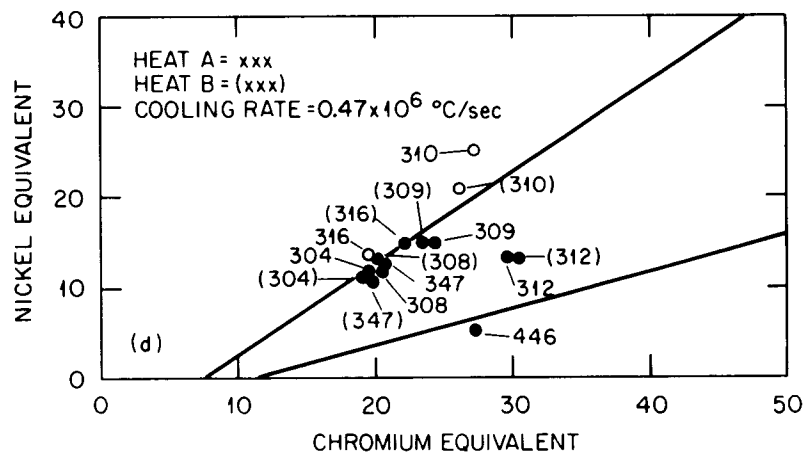
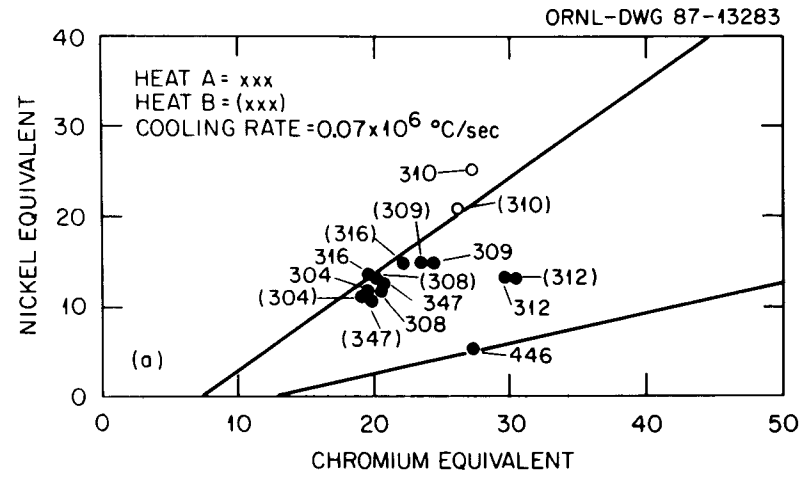
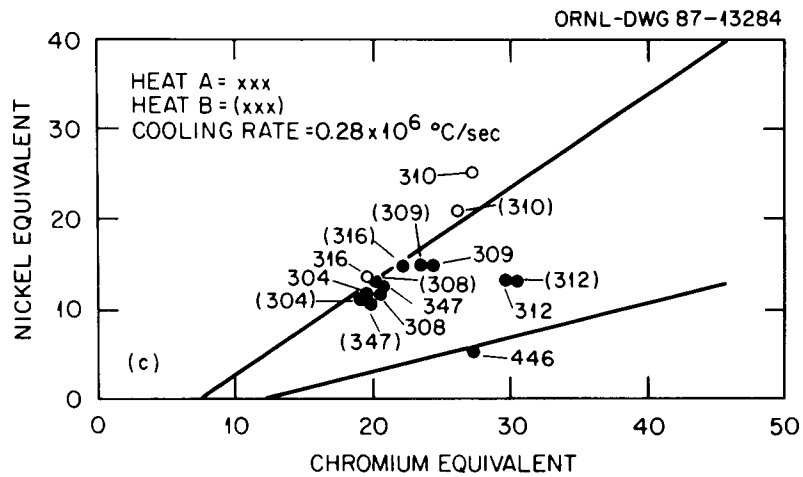


Fig. 15. Cooling rate modified Schaeffler diagrams showing the convergence of the 0 and 100% ferrite lines for the following cooling rates ($^{\circ}\text{C/s} \times 10^{-6}$) (a) 0.07, (b) 0.12, (c) 0.28, (d) 0.47, (e) 0.71, (f) 1.1, (g) 1.2, (h) 1.4, (i) 1.8, (j) 2.3. Open symbols represent single phase structures and filled symbols represent duplex structures.

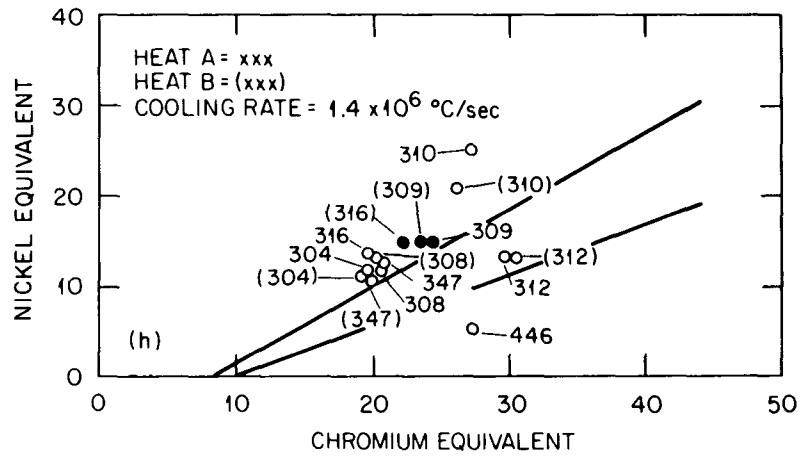
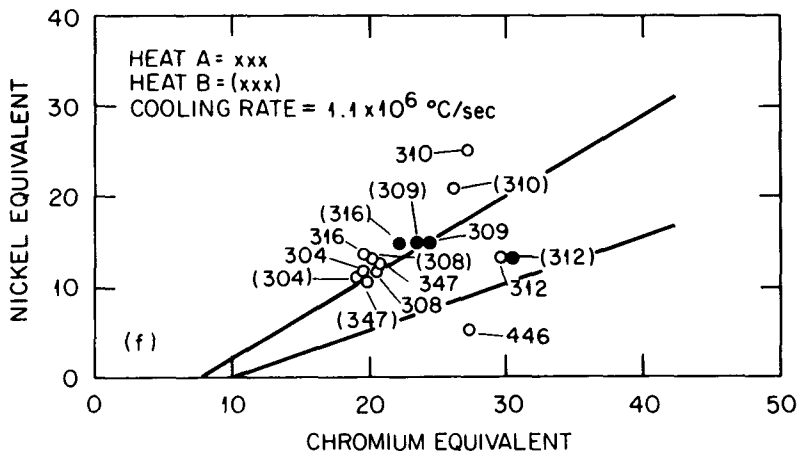
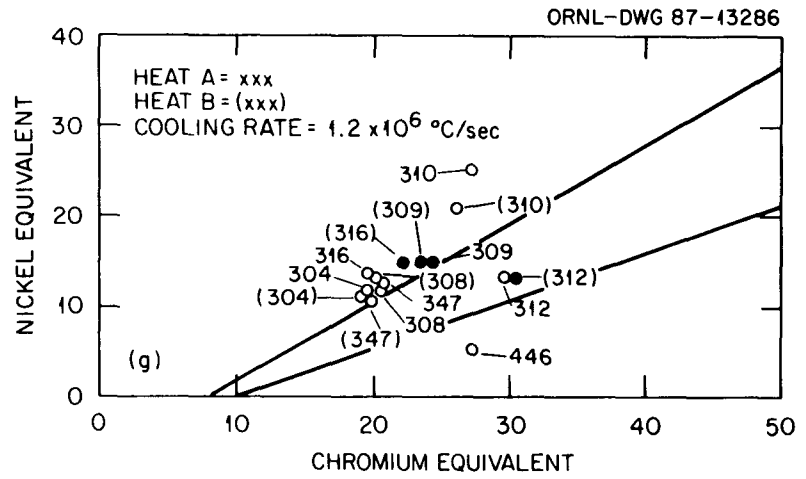
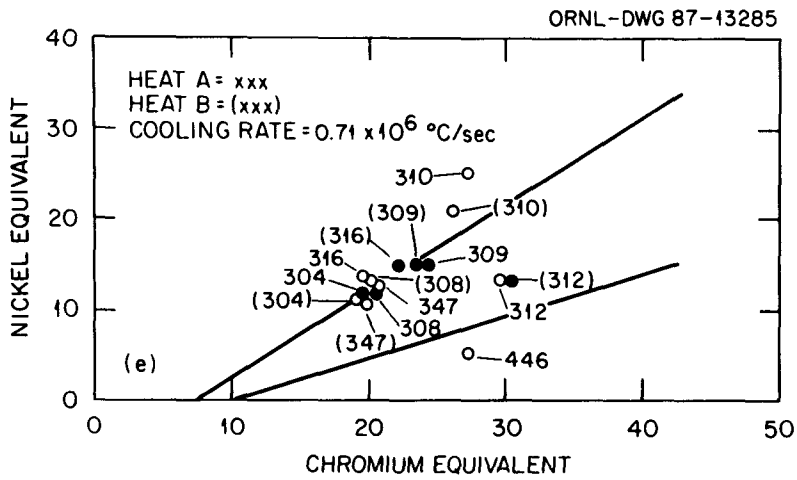


Fig. 15. (continued)

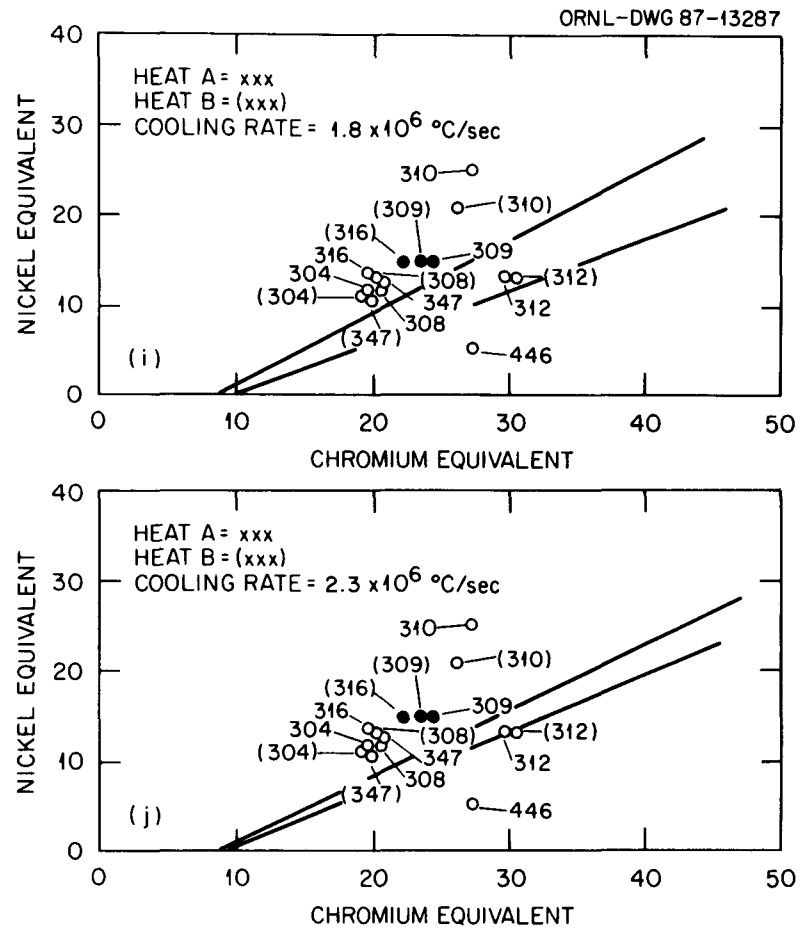


Fig. 15. (continued)

ORNL-DWG 86-18213R2

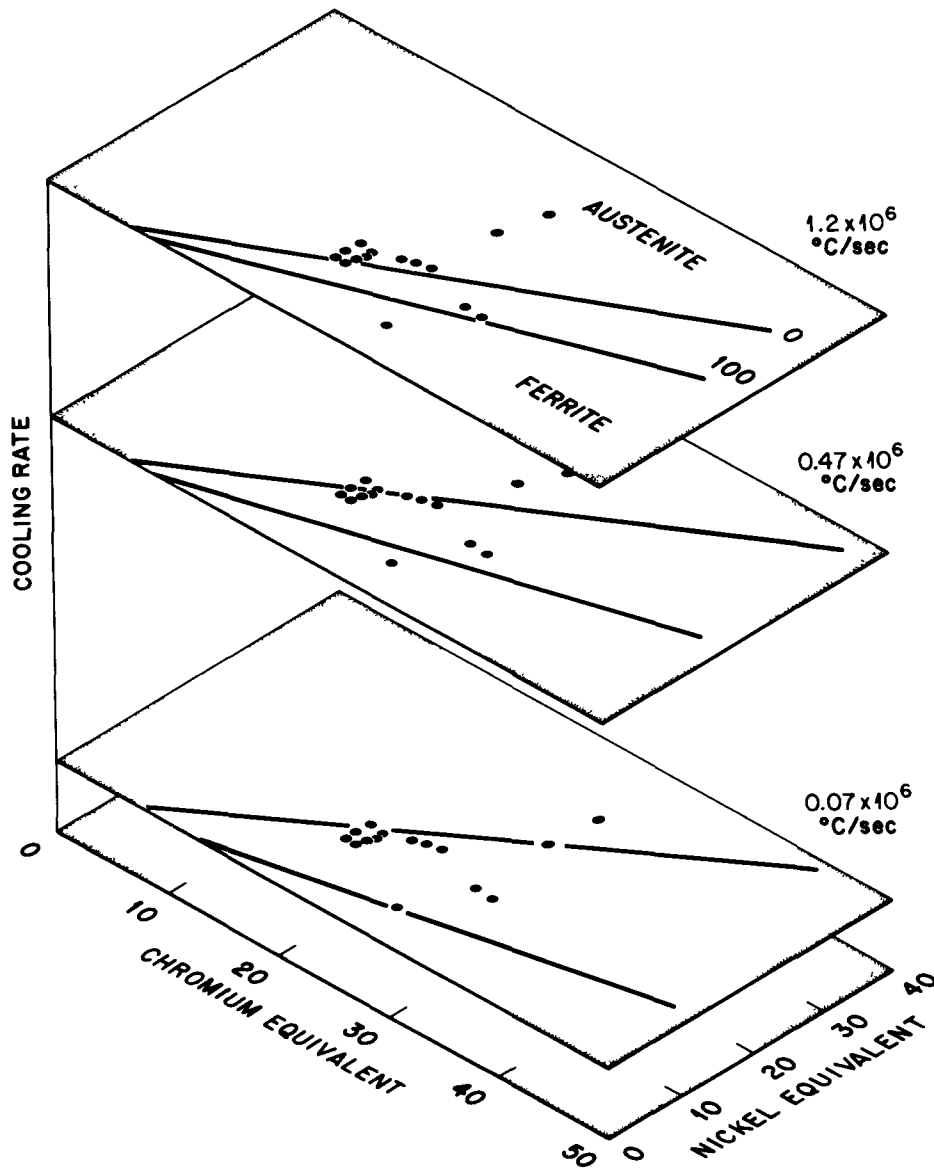


Fig. 16. Proposed composite constitution diagram for welds using cooling rate as a third dimension.

either deviating from straight contours, or by including several single phase austenite compositions into the two phase area, or moving the intersection of the 0 and 100% ferrite lines. Thus, it is apparent that a simple representation like the Schaeffler diagram does not work at all cooling rates. This may be an indication of one of several things. First, it is entirely possible that straight contour lines are an oversimplification and more complicated curves must be invoked. Alternatively, the restriction that the intersection of the 0 and 100% ferrite lines remains the same may be incorrect. It is also possible that the relations defining the nickel and chromium equivalents are inaccurate, at least at the higher cooling rates. It is quite possible that other, minor alloying additions must be incorporated into the nickel and chromium equivalent expressions, or that the coefficients are not optimal. This latter alternative is a very real possibility since several other expressions for the appropriate coefficients have been proposed.²³ At the present time we cannot ascertain which of these factors are dominant.

The possibility that the coefficients for the nickel and chromium equivalents need modification is supported by examining the dependence of the critical cooling rate for the transition to a fully austenitic structure on the Cr_{eq}/Ni_{eq} ratio. Given the calculated cooling rates in Table 2, one can arrive at upper and lower bounds for the critical cooling rates necessary to yield a fully austenitic structure. These ranges for the critical cooling rates have been plotted as a function of the Cr_{eq}/Ni_{eq} ratio in Fig. 17. For equivalent ratios of 1.4 to 1.8, a reasonable monotonic dependence of critical cooling rate on equivalent ratio for alloys 304A, 304B, 308A, 308B, 316A, and 347A is found. However, this relation breaks down for 347B, at higher chromium to nickel equivalent ratios as well as for alloys 309A and 309B, and 316B. It seems apparent that modifications to the formulas for calculating the nickel and chromium equivalents must be made in order to achieve any kind of reasonable relationship between composition and critical cooling rate.

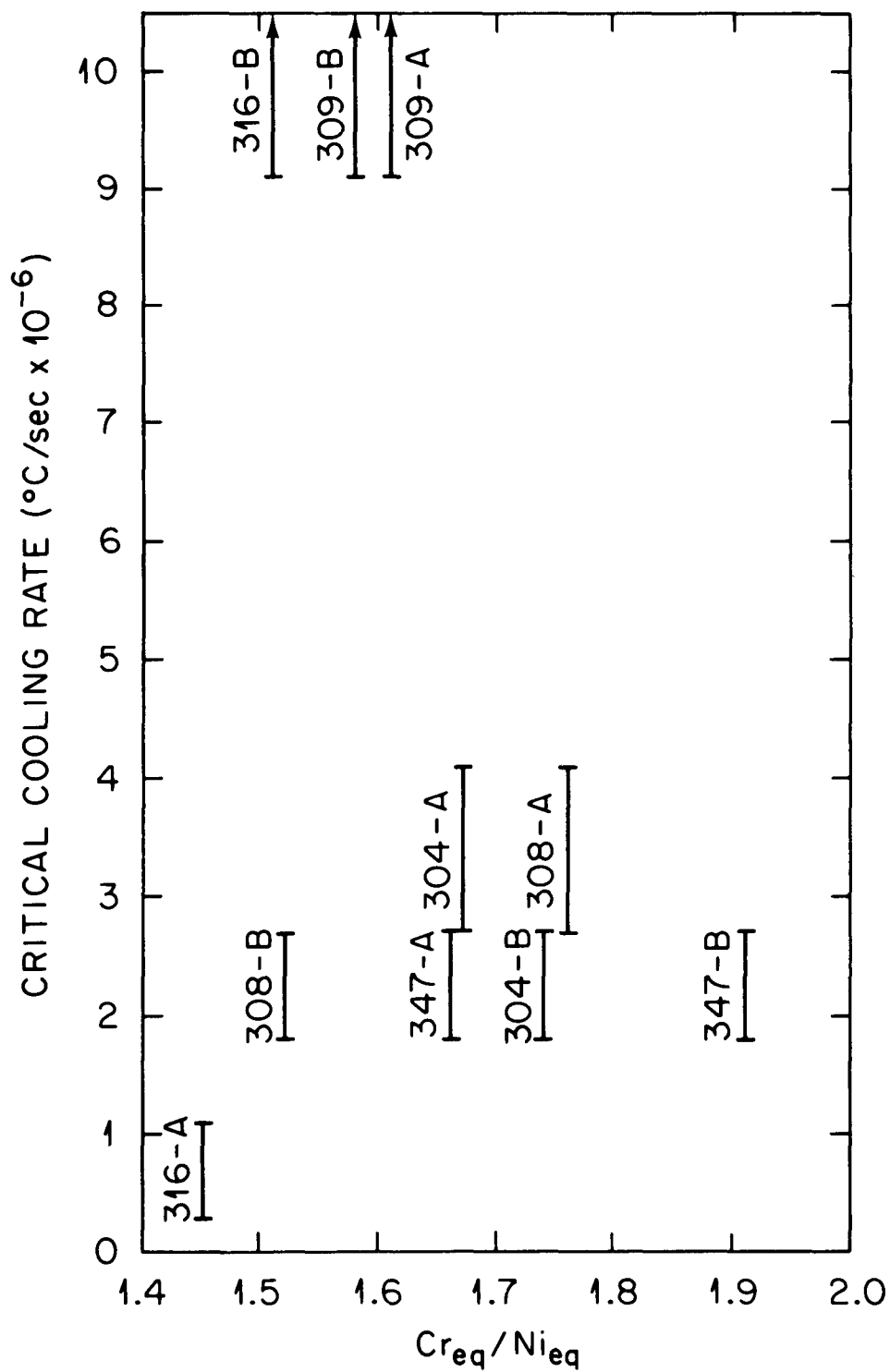


Fig. 17. Estimated range of critical cooling rates for the transition to fully austenitic microstructures as a function of $\text{Cr}_{\text{eq}}/\text{Ni}_{\text{eq}}$ ratio for several austenitic stainless steels.

CONCLUSIONS

A wide variety of austenitic stainless steel laser welds were made at various welding speeds to cover a range of weld metal cooling rates. The microstructures were evaluated and the results and conclusions are summarized as follows.

1. Rapid solidification of austenitic stainless steel weld metals show extensive modifications in their microstructures. The microstructures ranged from duplex $\gamma + \delta$ to fully austenitic and fully ferritic. The microstructures were cooling rate and composition sensitive.

2. Fully austenitic microstructures were produced in types 304, 308, 347, and 316 (heat A) laser welds that are otherwise duplex $\gamma + \delta$ after conventional welding. All of these steels showed a decrease in ferrite level with increase in laser welding speed or corresponding cooling rates.

3. Fully ferritic microstructures were produced in steels with high Cr_{eq}/Ni_{eq} ratios such as types 312 and 446 steels, that are also otherwise duplex $\gamma + \delta$ after conventional welding.

4. Substantial variations in microstructures were found from heat to heat. While it was possible to produce a fully austenitic microstructure in one heat of type 316 steel (A) beyond a critical cooling rate, another heat (B) remained duplex $\gamma + \delta$ at all cooling rates.

5. Types 309A, 309B, and 316B were always found to be duplex under the conditions investigated. In these steels the ferrite content initially increased with increasing cooling rate and then decreased to a large extent. However, no fully austenitic microstructures were observed.

6. The observed microstructural modifications are mainly due to changes in the primary mode of solidification at large undercoolings and/or subsequent suppression of solid state transformations. The normally duplex steels that readily produce fully austenitic microstructures undergo a change in the mode of solidification from primary ferrite to primary austenite at high cooling rates and associated large undercoolings. The steels that are fully ferritic do not change the mode of

solidification from primary ferrite. However, because of the rapid cooling rates, the postsolidification ferrite to austenite solid state transformation is suppressed, resulting in a fully ferritic microstructure. In some steels evidence for a mixed austenite ferrite mode of solidification was also observed.

7. Cooling rate effects were incorporated into modifications of the Schaeffler diagram to reflect the observed changes at high cooling rates of the weld metal. The Cr_{eq} and Ni_{eq} as used in the Schaeffler diagram does not seem to fully describe the ferrite forming tendency as a function of cooling rate.

ACKNOWLEDGMENT

The authors would like to thank R. W. Reed for preparing the specimens and welding. They also thank J. F. King and J. A. Horton for reviewing the manuscript and Prof. T. DebRoy of Pennsylvania State University for assisting in the cooling rate calculations. Thanks are due to Kathy Gardner and Glenda Carter for preparing the manuscript.

REFERENCES

1. A. L. Schaeffler, "Construction Diagram for Stainless Steel Weld Metal," *Met. Prog.* **56**(5), 680-680B (1949).
2. W. T. DeLong, "Ferrite in Austenitic Stainless Steel Weld Metal," *Weld. J.* **53**(7), 273s-286s (1974).
3. F. C. Hull, "Delta Ferrite and Martensite Formation in Stainless Steels," *Weld. J.* **52**(5), 193s-203s (1973).
4. L. Pryce and K. W. Andrews, "Practical Estimation of Composition Balance and Ferrite Content in Stainless Steels," *J. Iron Steel Inst.* **195**, 415 (1960).
5. E. A. Schoeffler, "Constitution Diagram for Stainless Steel Castings," *Met. Prog. Data Book* 51 (1977).
6. S. A. David, and J. M. Vitek, "Solidification Behavior and Microstructural Analysis of Austenitic Stainless Steel Laser Welds," pp. 247-54 in *Lasers in Metallurgy*, eds. K. Mukherjee and J. Mazumder, TMS-AIME, Warrendale, Penn., 1982.

7. J. M. Vitek, A. Das Gupta, and S. A. David, "Microstructural Modification of Austenitic Stainless Steels by Rapid Solidification," *Metall. Trans.* **14A**, 1833-41.
8. S. Katayama and A. Matsunawa, "Solidification Microstructures of Laser Welded Stainless Steels," *Proc. ICALEO 84*, Vol. 44, L.1.A, pp. 60-67, 1983.
9. T. F. Kelly, M. Cohen, and J. B. VanderSande, "Rapid Solidification of a Droplet-Processed Stainless Steel," *Metall. Trans.* **15A**, 819-823 (1984).
10. M. MacIssac, Y. Shiohara, M. G. Chu, and M. C. Flemings, "Structure of Undercooled Iron and Nickel Based Alloys," *Grain Refinement in Castings and Welds*, eds. G. J. Abbaschian and S. A. David, TMS-AIME, Warrendale, Penn., pp. 87-95.
11. T. W. Eagar, Massachusetts Institute of Technology, Cambridge, Mass., private communication to S. A. David, September 1982.
12. C. M. Adams, Jr., "Cooling Rates and Peak Temperatures in Fusion Welding," *Weld. J.* **37**(5), 210s-215s (1958).
13. P. A. A. Khan and J. DebRoy, "Absorption of CO₂ Laser Beam by A151 4340 Steel," *Metall. Trans. B* **16B**, 853-856 (1985).
14. D. M. Kroeger, W. A. Coghlan, D. S. Easton, C. C. Koch, and J. O. Scarbrough, "A Study of Cooling Rates During Metallic Glass Formation," *J. Appl. Phys.* **53**, 1445-53 (1982).
15. L. S. Weinman and J. N. Devault, "A Microprobe Study of Rapidly Solidified Laser Surface Alloyed Low Carbon Steels," pp. 239-42 in *Laser-Solid Interactions and Laser Processing-1978*, eds. S. D. Ferris, H. J. Leamy and J. M. Peate, American Institute of Physics, New York, 1979.
16. N. Suutala, "Solidification Studies on Austenitic Stainless Steels," *Acta Universitatis Ouluensis*, Series C, Technica No. 23, Metallurgica No. 3, University of Oulu, Finland, 1982.
17. S. A. David, D. N. Braski, and G. M. Goodwin, "Solidification Behavior of Austenitic Stainless Steel Filler Metals," *Weld. J.* **58**(11), 330s-336s (1979).

18. V. P. Kujanpää, S. A. David, and C. L. White, "Formation of Hot Cracks in Austenitic Stainless Steel Welds - Solidification Cracking," *Weld. J.* **65**(8), 203s-212s (1986).
19. R. Mehrabian, "Rapid Solidification," *Int. Met. Rev.* **27**, 185-208 (1982).
20. A. K. Jena, B. C. Giessen, M. B. Bever, and N. J. Grant, "The Metastability of Gold-Antimony Phases Prepared by Splat Cooling," *Acta Met.* **16**, 1047-1051 (1968).
21. N. Suutala, "Effect of Solidification Conditions on the Solidification Mode in Austenitic Stainless Steels," *Met. Trans.* **14A**, 191-197 (Feb. 1983).
22. J. C. Lippold, "Centerline Cracking in Deep Penetration Electron Beam Welds in Type 304L Stainless Steel," *Weld. J.* **64**(5), 127s-136s (May 1985).
23. N. Suutala, "Effect of Manganese and Nitrogen on the Solidification Mode in Austenitic Stainless Steel Welds," *Metall. Trans.* **13A**, 2121-2130 (1982).

INTERNAL DISTRIBUTION

- | | | | |
|--------|-------------------------------|--------|-----------------------------|
| 1-2. | Central Research Library | 29. | P. J. Maziasz |
| 3. | Document Reference Section | 30. | R. W. McClung |
| 4-5. | Laboratory Records Department | 31. | H. E. McCoy, Jr. |
| 6. | Laboratory Records, ORNL RC | 32. | R. K. Nanstad |
| 7. | ORNL Patent Section | 33. | A. R. Olsen |
| 8. | J. Bentley | 34-38. | R. W. Reed |
| 9. | J. A. Carpenter, Jr. | 39. | G. M. Slaughter |
| 10-14. | S. A. David | 40. | R. E. Stoller |
| 15. | J. H. DeVan | 41. | R. W. Swindeman |
| 16. | G. M. Goodwin | 42-46. | J. M. Vitek |
| 17-21. | T. L. Hebble | 47-49. | P. T. Thornton |
| 22. | D. O. Hobson | 50. | M. H. Yoo |
| 23. | J. A. Horton, Jr. | 51. | G. Y. Chin (Consultant) |
| 24. | J. R. Keiser | 52. | H. E. Cook (Consultant) |
| 25. | E. A. Kenik | 53. | F. F. Lange (Consultant) |
| 26. | O. F. Kimball | 54. | T. E. Mitchell (Consultant) |
| 27. | J. F. King | 55. | W. D. Nix (Consultant) |
| 28. | R. T. King | 56. | J. C. Williams (Consultant) |

EXTERNAL DISTRIBUTION

57. EG&G Idaho, Inc., P.O. Box 1625, Idaho Falls, ID 83415
J. Seydel, Branch Manager
58. Ford Motor Company, Dearborn, MI 48121
A. D. Brailsford
59. General Electric Research and Development Center,
Schenectady, NY 12301
W. Johnson
60. Idaho National Engineering Laboratory, 550 2nd Street,
Idaho Falls, ID 83415
D. D. Keiser
- 61-62. Lawrence Berkeley Laboratory, Materials and Molecular Research
Division, Berkeley, CA 94720
J. W. Morris, Jr.
N. E. Phillips

63. Lawrence Livermore National Laboratory, University of California,
P.O. Box 808, Livermore, CA 94550
Glen Mara
64. Los Alamos Scientific Laboratory, P.O. Box 1663,
Los Alamos, NM 87545
S. S. Hecker
65. National Bureau of Standards, Gaithersburg, MD 20899
S. J. Dapkunas
66. Office of Naval Research, Metals and Ceramics Program, Code 471,
800 N. Quincy, Arlington, VA 22217
R. C. Pohanka
- 67-73. DOE, Division of Materials Sciences, Washington, DC 20545
J. B. Darby (ER-131, J321/GTN)
R. J. Gottschall (ER-131, J321/GTN)
L. C. Ianniello (ER-13, J317/GTN)
R. H. Kropschot (ER-10, J304/GTN)
F. V. Nolfi (ER-131, J314/GTN)
D. K. Stevens (ER-11, J304/GTN)
M. C. Wittels (ER-132, J325/GTN)
74. DOE, Oak Ridge Operations Office, P.O. Box E, Oak Ridge, TN 37831
Office of Assistant Manager for Energy Research
and Development
- 75-202. DOE, Technical Information Center, Office of Information Services,
P.O. Box 62, Oak Ridge, TN 37831

For distribution as shown in DOE/TIC-4500, Distribution
Category UC-25 (Materials).